THE SEISMICITY OF MARS

D. Giardini[1], P. Lognonné[2,3], W. B. Banerdt[4], W. T. Pike[5], U. Christensen[6], S. Ceylan[1], J. F. Clinton[7], M. van Driel[1], S. C. Stähler[1], M. Böse[1,7], R. F. Garcia[8], A. Khan[1,9], M. Panning[4], C. Perrin[3], D. Banfield[10], E. Beucler[11], C. Charalambous[5], F. Euchner[1], A. Horleston[12], A. Jacob[3], T. Kawamura[3], S. Kedar[4], G. Mainsant[8], J.-R. Scholz[6], S. E. Smrekar[4], A. Spiga[2,13], C. Agard[14], D. Antonangeli[15], S. Barkaoui[3], E. Barrett[4], P. Combes[14], V. Conejero[3], I. Daubar[4], M. Drilleau[3], C. Ferrier[14], T. Gabsi[3], T. Gudkova[16], K. Hurst[4], F. Karakostas[17], S. King[18], M. Knapmeyer[19], B. Knapmeyer-Endrun[20], R. Llorca-Cejudo[14], A. Lucas[3], L. Luno[14], L. Margerin[21], J. B. McClean[5], D. Mimoun[8], N. Murdoch[4,8], F. Nimmo[22], M. Nonon[14], C. Pardo[3], A. Rivoldini[23], J. A. Rodriguez Manfredi[24], H. Samuel[3], M. Schimmel[25], A. E. Stott[5], E. Stutzmann[3], N. Teanby[12], T. Warren[26], R. C. Weber[27], M. Wieczorek[28] & C. Yana[14]

Affiliations

1 Institute of Geophysics, Department of Earth Sciences, ETH Zurich, Zurich, Switzerland
2 Institut Universitaire de France, 1 rue Descartes, 75005 Paris, France
3 Université de Paris, Institut de physique du globe de Paris, CNRS, F-75005 Paris, France
4 Jet Propulsion Laboratory, California Institute of Technology, Pasadena, CA, USA
5 Department of Electrical and Electronic Engineering, Imperial College London, London, UK
6 Max Planck Institute for Solar System Research, Göttingen, Germany
7 Swiss Seismological Service (SED), ETH Zurich, Zurich, Switzerland
8 Institut Supérieur de l'Aéronautique et de l'Espace SUPAERO, Toulouse, France
9 Institute of Theoretical Physics, University of Zurich, Zurich, Switzerland.
10 Cornell Center for Astrophysics and Planetary Science, Cornell University, Ithaca, New York, USA
11 Laboratoire de Planétologie et Géodynamique, Univ. Nantes, Univ. Angers, Nantes, France
12 School of Earth Sciences, University of Bristol, Bristol, UK
13 Laboratoire de Météorologie Dynamique, Sorbonne University, Paris, France
14 Centre National d'Etudes Spatiales, Toulouse, France
15 Institut de minéralogie, de physique des matériaux et de cosmochimie, Muséum National d'Histoire Naturelle, Sorbonne University, Paris
16 Schmidt Institute of Physics of the Earth, Russian Academy of Sciences, Moscow, Russia
17 Department of Geology, University of Maryland, College Park, MD, USA
18 Department of Geosciences, Virginia Polytechnic Institute, Blacksburg, VA, USA
19 DLR Institute of Planetary Research, Berlin, Germany

20 Bensberg Observatory, University of Cologne, Bergisch Gladbach, Germany
21 Institut de Recherche en Astrophysique et Planétologie, Université Toulouse III Paul Sabatier, CNRS, CNES, Toulouse, France
22 Dept. of Earth and Planetary Sciences, University of California Santa Cruz, Santa Cruz, CA, USA
23 Royal Observatory of Belgium, Brussels, Belgium
24 Centro de Astrobiologia - Instituto Nacional de Tecnica Aeroespacial, Madrid, Spain
25 The Institute of Earth Sciences Jaume Almera of the Spanish Scientific Research Council (ICTJA-CSIC), Barcelona, Spain
26 University of Oxford, Department of Physics, Oxford, UK
27 NASA Marshall Space Flight Center, Huntsville, AL, USA
28 Université Côte d'Azur, Observatoire de la Côte d'Azur, CNRS, Laboratoire Lagrange, France

The NASA mission *Interior Exploration using Seismic Investigations, Geodesy and Heat Transport* (InSight) landed on November 26, 2018 on Mars and completed the deployment of the *Seismic Experiment for Interior Structure* (SEIS) by the end of February 2019 on the surface of Elysium Planitia[1]. The SEIS goals are to detect, characterize and locate seismic activity on Mars and improve the knowledge of the internal structure, composition and dynamics of the red planet. The data recorded until September 30, 2019 reveal that Mars is seismically active: we recorded 174 marsquakes, with two distinct populations of seismic events, including small-magnitude events with waves propagating at crustal depth and over 20 marsquakes of magnitude Mw3-4 located below the crust and with waves propagating at different depths in the mantle. Marsquakes have spectral characteristics similar to those observed on the Earth and Moon. We draw the first map of seismicity of Mars, locating two of the larger events near the Cerberus Fossae system. We also obtain constraints on attenuation in crust and mantle, and indications for a potential S-wave shadow zone. This study is part of the first set of InSight science papers, [1] and [2] also include seismic data interpretation.

DETECTING AND CHARACTERIZING SEISMIC EVENTS ON MARS

Sol 185 was a typical sol on Mars (a Mars sol is 24h 39.5' long; we number sols starting from landing). The ground acceleration spectrogram recorded by the Very Broad Band (VBB) instrument of SEIS[3] (Fig. 1a) is dominated by the noise produced by the weakly turbulent night time winds and by the powerful, thermally-driven convective turbulence during the day[4]. Around 17:00 Local Mean Solar Time (LMST) the wind fluctuations die out quite suddenly and the planet remains very quiet into the early night hours. Several distinctive features can be seen every sol on Mars. Lander vibrations activated by the wind appear as horizontal thin lines with frequency varying daily as a result of temperature variations of the lander; almost invisible during quiet hours, they are not excited by seismic events (e.g. the lander mode at 4 Hz in Fig. 1a). We also observe a pronounced ambient resonance at 2.4 Hz, strongest on the vertical component, with no clear link to wind strength but excited by all the seismic vibrations at that frequency. The relative excitation of the 2.4 Hz and 4 Hz modes serve as discriminants for the origin of ground vibrations recorded by SEIS, allowing to distinguish between local vibrations induced by atmospheric or lander activity and more distant sources of ground vibrations. On Sol 185 two weak events can also be spotted in the quiet hours of the early evening, one with a broadband frequency content, a second 80 min later, centred on the 2.4 Hz resonance band (Fig. 1a).

In the combined image of sols 72 to 299 (Fig. 1b), the characteristic pattern of the wind noise and the events detected in the quiet evening hours can be tracked until September 30 (data were lost

during 20 sols of solar conjunction). The Marsquake Service (MQS; see the Methods section for all details and procedures) detected 174 events, classified into two main categories: (i) *low-frequency* (LF) events with energy content generally below 1Hz, including some events with a more broadband content extending up to the 2.4 Hz resonance; (ii) *high-frequency* (HF) events with energy above 1 Hz, reaching up to 6-12 Hz; smaller HF events can be seen only as narrow-band excitation of the 2.4 Hz ambient resonance. The 174 events detected until Sol 299 include 24 LF and 150 HF events, of which 131 are visible only as 2.4 Hz resonance events. Most events were detected during very quiet hours, devoid of recorded wind perturbations (Fig. 1b, Methods, SI1) and have small signal amplitudes with accelerations as low as 10^{-10} m/s^2. A distinct characteristic is the visible increase over this period in the rate of HF events, whereas LF events appear to take place at a more uniform rate. The full Mars seismic catalogue and waveform data are available from [5] and [6], respectively.

Once a suspected event is identified, the first critical step of the MQS processing is the discrimination between seismic energy and local spacecraft-, instrument- or atmospheric-induced perturbances (see Methods and Extended Data Fig. 1,2). Once we exclude an atmospheric or lander origin, we process each seismic event to determine P and S wave arrival times, distance, azimuth and magnitude[7–9]. Owing to the generally low signal-to-noise ratio (SNR), most seismic waveforms do not exhibit clear phase arrivals in the time domain, and the use of spectrograms and spectral envelopes have been the preferred method of both detection and investigation of seismic signals (Figs. 1a and 2)

The LF events display common characteristics. The signals have an overall duration of 10-20 minutes and most events show two distinct phases. Unambiguous P and S phase identification based on polarisation was possible only for the S0173a and S0235b events (Extended Data Fig. 3), and for the P phase for S0183a, as scattering prevents either positive or precise identification for all other events[2]. However, the similarity of the envelopes allows identification of the two phases as P and S for all events, in analogy to the waves observed for the larger events (Fig. 2). To date we have not positively identified other phases such as depth phases (i.e. pP, sP) or surface waves. No secondary P or S phases have been detected (e.g. PP, SS, PcP, ScS) and we assume in this analysis that the observed P and S are the direct phases.

The HF events also display common features (Fig 3b, 4b). The signal contains only HF energy with durations from 5-20 minutes, and most events show two separate peaks, interpreted as crustal P and S phases; a few events show only one dominant peak. The events observed as 2.4 Hz resonances have the same envelope shape as other HF events and we interpret them as low-amplitude HF events.

Extended Data Table 1 lists 13 LF and 23 HF events we use for further analysis in this paper. The SNR values of the selected LF events range from 2.5 to over 20, and peak-signal to peak-noise ratios range from 3.5 to over 200 (Extended Data Table 2).

ANALYSIS OF MARSQUAKES

The LF and HF events define two separate families, with different origin, source depth and wave paths, providing first evidence on the seismic activity, the seismic wave propagation and the internal structure of Mars.

Determination of distance for LF events and constraints on the radial mantle structure of Mars

The determination of epicentral distance using only one station and without sufficient knowledge of the internal velocity structure is challenging, especially with the lack of surface waves[10–12]. The MQS location procedure provides a probabilistic estimate of distance using an extensive *a priori* database of seismic velocity models, to capture the epistemic uncertainty related to our lack of knowledge of the interior of Mars (Supplementary Information SI2). The distance is then expressed as a Probability Density Function (PDF) spanning the whole set of models and a source depth varying between 0 and 100 km.

Even at this early stage, we can check the compatibility of each model with the recorded data and eliminate many models. In particular, over two thirds of the *a priori* models predict an extensive S-wave shadow zone starting around 20° distance and prove unable to match the S-P travel time differences measured for S0173a and S0235b; the allowed models tend to have a relatively thick crust (60-80 km) and a velocity increase or only a slight decrease below the Moho (Supplementary Information SI2).

LF event alignment and first indications for a low velocity zone in the mantle

Following in the tradition of classical seismology[13], we realign the events based on envelope similarity and using the travel-time curves of the a priori V_P and V_S models of Mars. We display in Fig. 3a the preferred alignment with time and distance, with the caveat that the alignment process is not always unique in case of low amplitude events.

Families of events with similar characteristics are recognized:

- Four events (S0235b, S0189a, S0105a, S0173a) with a dominant S phase, good P and S arrival picks and a robust distance assessment are closely packed in distance between 25° and 29° (displayed in light orange colour in the lower panel; see also the enlargement in Extended Data Fig. 4). Two events (S0185a, S0234c) with larger S-P travel time are located in the distance

range 58°-64°. All six events show P and S phases of similar characteristics, indicating a common seismic origin at different distances.

- Three events show a dominant P phase and only a small S phase (dark grey). For S0183a, we identify the P phase based on polarisation and, a weak S phase allows alignment of the event at around 46° distance. The shape of the P phase of S0205a indicates a very similar distance to S0183a. S0325a has mixed characteristics, with a similar P and a low amplitude S, at a distance of about 35°. The similarity with the P phases of the other events in the panel located at closer and further distance (see also Extended Data Fig. 4) points to a common seismic origin for all these events.
- The upper panel in Fig. 3a displays four events (S0167a, S0154a, S0133a, S0226b; light red) for which we see no clear P phase or only a small emergent P phase, affected by large uncertainty. In addition, the S phase related wave packet appears to be consistently longer than for the other events shown in the central panel. For these reasons, we conclude that these events are located further from the InSight station. The distance cannot be determined at this stage and we display the events aligned on a vertical line according to the S phase picks, to illustrate the envelope similarity. The longer duration may be due to the presence of reflected phases or surface waves in the scattered tail of the S wave.

The sequence of events with similar P-waves and dominant S-waves around 25°-30° and 58°-64° epicentral distance, separated by events with only a small S-wave at intermediate distance, provides the first evidence of a possible low velocity zone for S waves on Mars, located in the 40°-50° distance range (see also the detailed alignments of P and S phases in Extended Data Fig. 5). We explored alternative alignments, including the possibility that the decreasing S-wave amplitudes beyond 30° distance could be due to high attenuation in the deeper mantle below 300km depth. This model however is inconsistent with the high-amplitude S waves observed at farther distances.

LF spectral characteristics and the anelastic structure of Mars' mantle

The displacement spectrum of earthquakes[14]and moonquakes[15,16] can be commonly approximated by a constant term proportional to the event's seismic moment, modulated by attenuation terms accounting for the source dimension and the anelastic attenuation: $A(f) = A_0 A_{src}(f) A_{att}(f)$. We observe the same spectral shape also for the LF events recorded on Mars (Fig. 4a), providing a validation that the marsquake spectra obey similar scaling laws as quakes on the Earth and Moon.

Fig. 4a compares modelled spectra (in blue) to the observed vertical and average horizontal spectra (in red), compared with the noise spectra (in black). Using the magnitudes from the catalogue (see Methods) and the aligned distances (Fig. 3a) we achieve a consistent fit to the spectra, even for

those events barely above noise level. The spectral fit provides an independent distance estimation for events for which the alignment could not be determined; this is the case for S0167a, with a low-frequency spectral content compatible with a distance of over 120°.

Since the LF events in our catalogue have small magnitudes, their corner frequencies, a measure of the duration and size of the event, are above 1 Hz. As result, the decay of their spectra at high frequency is controlled by the attenuation term, and for each event we obtain an estimate of Q_{eff}, the effective attenuation parameter. Q_{eff} integrates contributions from scattering and intrinsic attenuation along the path and represents a lower bound on intrinsic Q. Since rays travel deeper with increasing epicentral distance, they sample different material properties than those seen by rays traveling in the lithosphere or upper layers of the mantle. The spectral fits of the events located at closer distance (Fig. 4a) are characterized by a Q_{eff} in the order of 300; the spectra of more distant events require instead a Q_{eff} in excess of 1000. This high value is consistent with the higher frequency content of these events, as illustrated by the broadband spectrum of S0185a, which reaches above 1 Hz and also shows also a 2.4 Hz resonance amplification. The Q_{eff} observed for the more distant events is high in comparison to pre-mission shear attenuation (Q_{μ}) estimates of 75-350 for the deep mantle[17–21]. However, these values derive from measurements of the tides raised on Mars by its closest moon Phobos, with a period of 5.55 hrs. The high value of the seismically observed Q_{eff} around periods of 1s effectively constrains the visco-elastic behaviour of Mars and is of particular importance for understanding its thermal and rheological structure[18,22,23].

Fig. 5 illustrates the schematic location of LF events below the Moho and the propagation of low-frequency waves across the mantle and the low-velocity zone.

Characteristics, crustal propagation and alignment of HF events

In Fig. 3b we align a selection of 23 HF with distance using the separation of P and S phases. The high-frequency content requires that these waves propagate in a low-attenuating medium, that appears to be different from the highly attenuating upper mantle traversed by the LF events at regional distance. We model the P and S wavepackets as multiply reflected Pg and Sg energy trapped in the crust or in the upper layers of the crust. The trapped waves travel with crustal velocities and the distance spans a wide range, which is still uncertain and depends on the assumed velocity and depth of reflection. The P-S travel time difference for the farthest HF event, S0264e, would correspond to an epicentral distance ranging from almost 60° for a full crustal propagation with V_S=4km/s to 10°-15° for a propagation in slow shallow layers with V_S=700-1000m/s. The distance and corresponding magnitude listed in Extended Data Table 1 are derived for an intermediate reference value of V_S=2km/s and V_P=1.73V_S.

The observation of trapped waves is directly linked to event depth, as they can only be excited by

events within the shallow crustal layers. This points to event depths in the crust for the HF events and below the Moho for the LF events. A mantle source for the LF events is also compatible with the absence of clearly developed surface waves.

The spectral plateau in Fig. 4b shows that the HF events are consistently smaller than the recorded LF events, and because of this any low-frequency content would be masked by noise. The corner frequency is typically around 6Hz, though for some events is as high as 10-12Hz. The possible contribution of the source duration is significant for these magnitudes at high frequency; however, a lower bound on attenuation on the propagation path in the crust or shallow layers can be derived by comparing model spectra incorporating both source and attenuation (blue lines in Fig. 4b) or only the attenuation decay (green lines) to the observed spectra (red lines). The high Q_{eff} values are compatible with the minimum Q_i values derived by [2] for Mars's shallowest layers. In Fig. 5, the schematic location of HF events in the crust and the propagation of multiply-reflected Pg and Sg phases is compared with the LF events.

Among the most surprising characteristics of the HF events is the non-stationarity of their occurrence. We have carefully evaluated the evolution of the ambient noise and of the detection capacity of SEIS since deployment and can rule out that the increase in HF events occurrence is an artefact. We are evaluating possible causative models to explain a time-dependent, possibly seasonal, release of these quakes, related e.g. to orbital or thermal effects. Some of these models would indicate a very shallow origin of these events, which in turn could also indicate a closer epicentral distance.

Geographical distribution of seismicity on Mars

We can use the locations of the LF events to explore the geographical distribution of the observed seismicity, taking into account that we retrieved complete locations only for three events so far, and that for the other events only the distance could be assessed.

In Fig. 6 we locate the events on the map of the planet: S0235b, S0173a and S0183a are shown with their PDF solution in distance and azimuth (see insert), while for the other events we identify four circular zones drawn around the InSight location, following the distance alignment obtained in Fig. 3a. This unconventional style of mapping is necessary until we can better constrain the azimuth of the events, but nevertheless makes it possible to compare the distance ranges with possible active tectonic systems.

In particular, the robust control on the location of the S0173a and S0235b events allows us to identify possible sources for these two marsquakes. Several major volcanic and tectonic structures are located near the InSight landing site (Supplementary Information SI4). The uncertainty bounds

of both events include the Cerberus Fossae region (insert in Fig. 6). These fossae were associated with possible recent volcanic activity[24] and have been previously identified as a large potentially active extensive tectonic structure close to InSight[25], where relatively fresh boulder traces hint at constant seismic activity[26]. The possible association of S0173a and S0235b to the active system of the Cerberus Fossae provides a strong indication that tectonic stress localization, in addition to thermo-elastic cooling, may play an important role in the genesis of seismicity on Mars.

Aftershocks

A common pattern in Earth's seismicity is the occurrence of aftershocks with similar characteristics to the mainshock. The first aftershock tentatively identified by MQS is S0235c, a small-magnitude event following 35 min after the much larger S0235b event, with similar spectral characteristics, further supporting the marsquake nature of the seismic events on Mars.

A good start

Over 44 years since the first attempt by the Viking missions[27], the InSight SEIS instrument has revealed that Mars is seismically active. In the first 207 sols of data continuously recorded on Mars we detected 174 events which cannot be explained by local atmospheric- or lander-induced vibrations, and are interpreted as marsquakes. We identify two families of marsquakes: (i) 24 events of magnitude M_W=3-4, located below the crust and with waves traveling inside the mantle, and (ii) 150 events of smaller magnitude and of closer distance, with waves trapped in the crust.

It is possible that a different type of source might explain individual seismic events. Alternative mechanisms which are being explored include: meteorite impacts[28], infrasonic waves trapped in near-surface waveguides[29], episodes of underground fluid migration, and gravitational phenomena such as mass wasting along impact crater walls in the vicinity of the landing site.

The first seismic observations on Mars deliver key new knowledge on the internal structure, composition and dynamics of the red planet, opening a new era for planetary seismology.

1. Banerdt, W. B. et al. Early Results from the InSight Mission: Mission Overview and Global Seismic Activity. *Nat. Geosci.*
2. Lognonné, P. et al. First constraints on the shallow elastic and anelastic structure of Mars from InSight data. *Nat. Geosci.* (2020).
3. Lognonné, P. *et al. SEIS: Insight's Seismic Experiment for Internal Structure of Mars*. *Space Science Reviews* vol. 215 (2019).
4. Banfield, B. et al. The Atmosphere of Mars as Observed by InSight. *Nat. Geosci.* (2020).
5. InSight Marsquake Service (2020). Mars Seismic Catalogue, InSight Mission; V1 2/1/2020. ETHZ, IPGP, JPL, ICL, ISAE-Supaero, MPS, Univ Bristol. Dataset. 10.12686/a6
6. InSight Mars SEIS data Service (2020). SEIS raw data, InSight Mission. IPGP, JPL, CNES, ETHZ, ICL, MPS, ISAE-Supaero, LPGN, MSFC. Other/Seismic Network. 10.18715/SEIS.INSIGHT.XB_2016
7. Böse, M. *et al.* Magnitude Scales for Marsquakes. *Bull. Seismol. Soc. Am.* **108**, 2764–2777 (2018).
8. Böse, M. *et al.* A probabilistic framework for single-station location of seismicity on Earth and Mars. *Phys. Earth Planet. Inter.* **262**, 48–65 (2017).
9. Clinton, J. *et al. The Marsquake Service: Securing Daily Analysis of SEIS Data and Building the Martian Seismicity Catalogue for InSight*. *Space Science Reviews* vol. 214 (2018).
10. Panning, M. P. *et al.* Verifying single-station seismic approaches using Earth-based data: Preparation for data return from the InSight mission to Mars. *Icarus* (2015) doi:10.1016/j.icarus.2014.10.035.
11. Khan, A. *et al.* Single-station and single-event marsquake location and inversion for structure using synthetic Martian waveforms. *Phys. Earth Planet. Inter.* **258**, 28–42 (2016).
12. van Driel, M. *et al.* Preparing for InSight: Evaluation of the Blind Test for Martian Seismicity. *Seismol. Res. Lett.* **90**, (2019).
13. H. Jeffreys; Bullen, K. E. *Seismological tables*. (Office of the British Association for the Advancement of Science, 1940).
14. Brune, J. N. Tectonic stress and the spectra of seismic shear waves from earthquakes. *J Geophys Res* (1970) doi:10.1029/jb075i026p04997.
15. Kawamura, T., Lognonné, P., Nishikawa, Y. & Tanaka, S. Evaluation of deep moonquake source parameters: Implication for fault characteristics and thermal state. *J. Geophys. Res. Planets* (2017) doi:10.1002/2016JE005147.
16. Oberst, J. Unusually high stress drops associated with shallow moonquakes. *J. Geophys. Res.* **92**, 1397 (1987).
17. Bills, B. G., Neumann, G. A., Smith, D. E. & Zuber, M. T. Improved estimate of tidal dissipation within Mars from MOLA observations of the shadow of Phobos. *J. Geophys. Res. E Planets* (2005) doi:10.1029/2004JE002376.
18. Khan, A. *et al.* A Geophysical Perspective on the Bulk Composition of Mars. *J. Geophys. Res. Planets* (2018) doi:10.1002/2017JE005371.
19. Lognonné, P. & Mosser, B. Planetary seismology. *Surv. Geophys.* (1993) doi:10.1007/BF00690946.
20. Smrekar, S. E. *et al.* Pre-mission InSights on the Interior of Mars. *Space Science Reviews* (2019) doi:10.1007/s11214-018-0563-9.
21. Zharkov, V. N. & Gudkova, T. V. Construction of Martian interior model. *Solar System Research* (2005) doi:10.1007/s11208-005-0049-7.
22. Bagheri, A., Khan, A., Al-Attar, D., Crawford, O. & Giardini, D. Tidal Response of Mars Constrained From Laboratory-Based Viscoelastic Dissipation Models and Geophysical Data. *J. Geophys. Res. Planets* (2019) doi:10.1029/2019JE006015.
23. Nimmo, F. & Faul, U. H. Dissipation at tidal and seismic frequencies in a melt-free, anhydrous Mars. *J. Geophys. Res. E Planets* (2013) doi:10.1002/2013JE004499.
24. Vaucher, J. *et al.* The morphologies of volcanic landforms at Central Elysium Planitia: Evidence for recent and fluid lavas on Mars. *Icarus* (2009) doi:10.1016/j.icarus.2008.11.005.

25. Taylor, J., Teanby, N. A. & Wookey, J. Estimates of seismic activity in the cerberus fossae region of mars. *J. Geophys. Res. E Planets* (2013) doi:10.1002/2013JE004469.
26. Brown, J. R. & Roberts, G. P. Possible Evidence for Variation in Magnitude for Marsquakes From Fallen Boulder Populations, Grjota Valles, Mars. *J. Geophys. Res. Planets* (2019) doi:10.1029/2018JE005622.
27. Anderson, D. L. *et al.* Seismology on Mars. *J. Geophys. Res.* **82**, 4524–4546 (1977).
28. Daubar, I. *et al.* Impact-Seismic Investigations of the InSight Mission. *Space Science Reviews* (2018) doi:10.1007/s11214-018-0562-x.
29. Garcia, R. F. *et al.* Finite-Difference Modeling of Acoustic and Gravity Wave Propagation in Mars Atmosphere: Application to Infrasounds Emitted by Meteor Impacts. *Space Science Reviews* (2017) doi:10.1007/s11214-016-0324-6.
30. Knapmeyer, M. *et al.* Working models for spatial distribution and level of Mars' seismicity. *J. Geophys. Res. E Planets* (2006) doi:10.1029/2006JE002708.

Table and figure captions

Fig 1. a, Spectrogram for Sol 185, showing acceleration data recorded at 20 samples-per-second for the vertical VBB component. We mark (A) two modes excited by atmospheric perturbations and lander-ground coupling, (B) the 2.4Hz ambient resonance mode, which continuously exists throughout the day, (C) the two seismic events S0185a and S0185b detected on Sol 185. **b,** Stack of spectrograms for sols 72-299. Each horizontal line corresponds to a sol-long acceleration spectrogram from 20s to 4Hz for the vertical VBB component. White spaces indicate data gaps. The 174 detected events are marked, with symbols corresponding to the event type, while event quality is indicated with colour.

Fig 2. Spectral envelopes and acceleration power spectrograms for 10 LF (**a**) and 6 HF (**b**) events. Vertical dashed lines indicate the signal start and end times selected by MQS for the events, while vertical solid lines show the picked P and S seismic phases where available. The frequency band used for each event, shown with horizontal dashed lines, is manually picked to isolate the useful signal. Envelopes are computed by summing the spectral amplitudes over frequency. The spectrograms are calculated using window lengths of 60 s and 80 s for LF and HF events, respectively with an overlap of 50%. Glitches are removed from the spectral envelopes for visual clarity.

Fig 3. Event alignment guided by spectral envelope similarity for LF events in **a** and HF events in **b**, using the vertical component. Events in the bottom panel in **a** are aligned in distance by matching their P- and S-wave envelopes, with the exception of S0205a where we observe only P phase. Vertical grey line in the top panel is used as reference to align the S-wave envelopes only. HF events in **b** are aligned using theoretical Pg and Sg group arrivals to show relative distribution of these events in distance. Greyed-out portions of envelopes indicate glitches.

Fig 4. Displacement spectra of all events in Fig. 2 (red), compared to pre-event noise (black). The spectra are compared to a prediction using a Brune source spectrum for a stress drop of 1 MPa with an attenuation term using an effective quality factor Q_{eff} and a representative distance (blue, dashed). For the HF events, the green dashed line shows a predicted spectrum purely from attenuation, with a flat source spectrum. The spectra are displayed for the vertical and average horizontal components. Time windows used for computation of the spectra are given in Table SI3.1.

Fig 5. Schematic of wave propagation for the different event types. HF events excite trapped waves in the crust while mantle waves are attenuated below the noise level. LF events are stronger, cannot excite trapped waves as they are located below the Moho and the mantle waves are observed at long periods due to attenuation. A potential low velocity layer (LVL) may explain the observed distance variation of S-wave amplitudes.

Fig 6. Global seismicity map of Mars shown on a Mars Orbiter Laser Altimeter (MOLA) elevation map. White shaded bands are range of epicentral distances. Red to yellow ellipsoids are the estimated locations of events S0173a and S0235b; the estimated location of S0183a is displayed with two shaded ellipses, representing distance uncertainties of 5° and 10°. The insert to the right shows a map view on the epicentral area of the three event locations relative to the InSight landing site (yellow triangle), and associated with main surface fault traces for Cerberus Fossae, where black and red lines are main reverse and normal mapped faults, respectively (modified from [30]).

Methods: MQS procedures for event detection, event characterisation and catalogue management

SEIS data is retrieved by SISMOC (SEIS on Mars Operations Center) on Earth, prepared for analysis and automatically delivered to both the MSDS (Mars SEIS Data Service) for distribution to the InSight science team and to the Marsquake Service (MQS). The MQS is tasked with analysis of the SEIS dataset and curation of the marsquake catalogue, reacting every day as new data are downloaded from Mars[9]. MQS frontline seismologists on duty are charged with initial data screening and preliminary event characterization. The MQS review team routinely convenes to confirm the frontline analysis.

SEISMIC EVENT DETECTION AND DISCRIMINATION

Once the MQS frontline person on duty is informed that there is new data available, the search for marsquakes begins. Seismic events identified so far are characterised by energy between ~0.1-10Hz, durations ranging from 5-30 minutes, and typically have amplitudes only slightly above the lowest background noise, which occurs only for a few hours each sol. We automatically produce spectrograms for each sol and all channels, updated with each new data arrival. The seismologist on duty scans through time series and spectrograms looking for features within this energy band to identify any candidate seismic signals, and then works to ensure the signal cannot be explained by any non-seismic phenomena. We take the example of Sol 189, during which a typical event occurs, to illustrate our detection and discrimination procedures.

1. Detection and first discrimination: The sol-long spectrogram from the VBB vertical component spectrogram is shown in the top part of (a) in Extended Data Fig. 1. A candidate seismic band of energy is visible in the middle of the quietest period, the lower part of (a) shows the spectrogram zoomed into this period, with event energy start and end times as identified by MQS. Panels (b) and (c) show various waveforms from the same zoomed time period. (b) presents the three-components of VBB velocity seismograms filtered between 1.2s – 2.8s. (c) displays the auxiliary channels for pressure (detrended), wind direction and wind speed, and the 3 magnetic channels. In addition, MQS has access to known spacecraft activity, such as robotic arm movement and lander communication. These datasets are always checked to ensure there are no anomalous atmospheric or lander signals that correlate with seismic signals. In this case, there is lander communication activity (UHF radio transmission) that clearly affects the magnetic channels (shaded grey area in (c)), but this concludes some minutes before the seismic energy starts. There is no indication of an anomalous signal in the pressure signal, and for the

majority of the signal, the wind speed is at or below the sensitivity of the TWINS instrument (2.8 m/s). Further, there is no visible wind excitation of lander modes.

2. Direct comparison of wind and seismic data: Since the amplitudes of the seismic signals are generally very small and only just above the background noise within a relatively narrow frequency band, wind contamination is of particular concern. Extended Data Fig. 2 shows seismic and wind signals from a wider time window for Sol 189 (marked above the top panel of Extended Data Fig. 1). Significant wind speed and direction changes occur during the turbulent period, hours before the seismic energy begins. However, during the quieter period when this event occurs, the wind recorded by TWINS is mostly between 1.8 and 2.8 m/s, with wind bursts up to 3.5 m/s.

Following this set of analyses, MQS concludes the signal cannot be explained by atmospheric or lander signals and is of seismic origin. Once an event is confirmed, it is added into our database and it is labelled following the convention S[xxxx][z]; where [xxxx] indicates the InSight mission sol the event begins on (starting from Sol 0, the sol InSight landed on Mars), and [z] is a letter that ensures unique names if multiple events occur on a single sol. This particular event is assigned the event name of S0189a.

In the period following this first detection, various efforts continue to be made to understand the possible effects of weather on the observed seismic signal and provide estimates of the strength of the seismic signal. These methods are described in detail in Supplementary Information. 1, with application to the S0189a event.

SEISMIC EVENT CHARACTERISATION

Once an event is considered to be seismic, we proceed to characterisation, which is illustrated here using the LF event on Sol 235, S0235b, one of the largest events recorded so far. For all events, MQS will try to make a single station location for the event, which involves various stages:

1. Phase picking: we assign pick uncertainties that reflect the sharpness of observed energy onsets, guided both by the spectrogram, and if possible, also the filtered time series. Typically, for picks guided by the spectrogram, MQS selects uncertainties between ±10-60s; for picks that are directly visible in the time series, picks are selected on a single component and uncertainties are between ±1-2s. There are 2 picks made for S0235b, both with ±2s uncertainty, as shown on the velocity time series in Extended Data Fig. 1. At this stage, the phase type is not known, and according to IASPEI naming convention, the first onset energy phase is assigned to be x1, subsequent phases are x2 etc. For HF events, slope breaks on an STA-LTA filter centred on 2.4Hz is used to identify phases.

2. Phase polarisation: MQS also makes a polarisation analysis for degree of ellipticity, azimuth and inclination. For the majority of phases, there is no obvious polarisation. For the largest LF events, the polarisation is clear for a few seconds following the arrivals, before breaking down. Extended Data Fig. 1 provides the hodograms indicating the azimuth for each of the two identified arrivals for S0235b. For x1 on S0235b, the polarisation is 74°, x2 has clearly a different polarisation angle.
3. Phase association: In general, it is challenging to assign phase types to the arrivals. In the absence of clear polarisation, we infer and assign phases to x1 and x2 - P and S wave arrivals for LF events; Pg and Sg for HF events. In the case of S0235b, the clear change in polarisation provides additional indication that we are looking at P and S arrivals. The selected back azimuth for this event is 74 degrees, from the P wave train. So far, only first arriving P/Pg and S/Sg phases have been assigned to events.
4. Distance, back azimuth and location: Since S0235b has both P and S phases assigned, as well as a polarisation of the P-wave, following [8] and SI2, we can (1) calculate a preferred absolute distance of 26 degrees; (2) a back-azimuth of 74°; and location at 11°N, 161°E. For the majority of events, at most the distance can be provided.
5. Event type and quality are assigned to all events. The event type reflects the frequency content as discussed in the main text (Low Frequency (LF) and High Frequency (HF)). The event quality is assigned according to the following conventions:

   A – high quality events: multiple clear and identifiable phases and clear polarisation (i.e. location available)

   B – medium quality events: multiple clear and identifiable phases but no polarisation (distance available, but no azimuth and hence no unique location)

   C – low quality events: signal clearly observed but phase picking is challenging

   D – weak or suspicious events

   S0235b is classified as LF Quality A event.
6. Magnitudes are assigned according to scales tailored for Mars[7] with an updated calibration reflecting the actual data and observed events (Supplementary Information SI3). For each event several magnitudes are computed, depending on the availability of different phases. LF events observed so far are all in the magnitude range M_W3-4, while the more local HF events are in the range M_W1-2.3 (accounting also for the large uncertainty in distance). S0235b has magnitude M_W3.6.

FURTHER EVENT REVISION

All events are periodically revised according to the distance alignment procedure outlined in the main text. When phases are clear and impulsive, no changes or minimal re-alignments are made. For some events, major realignments are made, guided by waveform similarity, re-assignment of initial phase association or indications that phases are emerging and pick times do not correctly reflect the phase onset.

EVENT CATALOGUE

In the period up to Sol 299, over 174 events have been identified in the data. Extended Data Table 1 includes the key characteristics for the 36 LF and HF events, including S0189a and S0235b described above. We indicate pick times and uncertainties for P/Pg and S/Sg phases, and distances from both catalogue locations and realignment. The complete catalogue including all events is available at [5].

Data availability

The InSight seismic event catalogue[5] and waveform data[6] are available from the IPGP Datacenter and IRIS-DMC. Seismic waveforms as well as data from all other InSight instruments and MOLA topographic data are available from NASA PDS.

Acknowledgements

We acknowledge NASA, CNES and its partner agencies and Institutions (UKSA, SSO, DLR, JPL, IPGP-CNRS, ETHZ, IC, MPS-MPG) and the flight operations team at JPL, SISMOC, MSDS, IRIS-DMC and PDS for providing SEIS data.

The Swiss co-authors were jointly funded by (1) Swiss National Science Foundation and French Agence Nationale de la Recherche (SNF-ANR project 157133 "Seismology on Mars"), (2) Swiss State Secretariat for Education, Research and Innovation (SEFRI project "MarsQuake Service-Preparatory Phase") and (3) ETH Research grant ETH-06 17-02. Additional support came from the Swiss National Supercomputing Centre (CSCS) under project ID s992. The Swiss contribution in implementation of the SEIS electronics was made possible through funding from the federal Swiss Space Office (SSO), the contractual and technical support of the ESA-PRODEX office.

The French Team acknowledge the French Space Agency CNES which has supported and funded all SEIS related contracts and CNES employees as well as CNRS and the French team universities for personal and infrastructure supports. Additional support was provided by ANR (ANR-14-CE36-0012-02 and ANR-19-CE31-0008-08) and for IPGP team by UnivEarthS Labex program (ANR-10-LABX-0023), IDEX Sorbonne Paris Cité (ANR-11-IDEX-0005-0).

SEIS-SP development and delivery were funded by the UK Space Agency.

A portion of the work was carried out at the InSight Project at the Jet Propulsion Laboratory, California Institute of Technology, under a contract with the National Aeronautics and Space Administration.

The MPS SEIS team acknowledges the funding for the SEIS Leveling system development by the DLR German Space Agency.

We thank gempa GmbH for software development related to MQS tools.

This paper is InSight Contribution Number 102.

Authors' contributions

- DG coordinated the seismological interpretations and wrote the manuscript
- PL leads the SEIS experiment and the VBB sensor; he designed the higher-level requirements of the experiment together with DM
- WBB leads the InSight mission and the US contribution to SEIS
- DG, PL, WTP and UC lead SEIS subsystems

- SC, JFC, MvD, SCS contributed figures and to the writing of the main text and methods
- SC, JFC, SCS, MvD, MB, RFG, AK, MP, CP, PL and WTP provided seismological analyses
- JFC, MB, SC, CC, MvD, AH, AK, TK, GM, JRS and SCS comprise the Marsquake Service frontline team leading first data analysis; DG, WBB, DB, RFG, SK, PL, MP, WTP, SES, AS and RCW, in addition to the frontline team members, serve in the Marsquake Service review team
- FE leads the MQS operational software development, and EB, CP, SCS and SC manage Event Request Proposals
- AS and DB manage the Mars Weather Service
- DB and JRM lead the InSight APSS and TWINS instruments
- On-board flight software is coordinated by RLC and MN
- ID, NT and FK lead investigation into impacts, and AL and SK contribute on other non-seismic sources
- NM, KH, DM and BKE contribute to lander modes and noise
- Additional seismological contributions are from LM, ES, MD, MS and SB, TW and JMcL
- Martian velocity models and discussions are contributed by AK, AR, HS, TG, SK, FN and DA
- MSDS services are operated by CP and VC, while TG leads the VBB operations at IPGP and contributed to the tests and mars commissioning. LL, CF, CA and PC perform SISMOC ground services. EB contributes to SEIS operations and CY leads SEIS operations.
- Method is contributed by: JFC, SC, SCS, MvD, CC, WTP, PL
- Supplementary Information SI1-SI4 are contributed by: SI1: PL, RFG, WTP, CC, AES, SC, SCS; SI2: AK, AR, HS; SI3: MB, SCS; SI4: CP, AJ, MK

All authors read and commented on the manuscript.

Additional information

Supplementary Information is available for this paper. Correspondence and requests for materials should be addressed to DG.

Extended data figure and table captions

Extended Data Fig 1. Analysis of the seismic event observed on Sol 189. **a,** Acceleration spectrogram for entire sol (top) and zoom around the event (bottom) with event start and end times (UTC) marked. **b,** Three component seismic channels in m/s (VBB, 20 sps) with MQS phase picks and uncertainties. **c,** Auxiliary channels used when analysing the data. Timing of **b** and **c** match the bottom spectrogram in **a**. VBB is the very broadband seismometer, and MAG1/2/3 are the three magnetometer channels. The only lander activity during the event period (UHF communication) is marked with shaded area on the MAG channels. Time span shown in Extended Data Fig.2 is marked in the 24hour window at the top of **a**.

Extended Data Fig 2. Comparison of wind and seismic data in a 5-hour period centred around the seismic event on Sol 189. **a**, Wind speed (black) and direction (green), **b**, vertical 20sps VBB data with 1s high pass (blue) and 1s low pass (red) filters, **c** and **d**, spectrogram of seismic channel. The wind speed is below 2.8 m/s for the majority of the seismic event, as it is for much of quiet evening period. While a wind direction change of 30 degrees was recorded during the event by the TWINS sensor, the longer context shows that this is occurring about once per hour and is likely an artefact of the sensor at very low wind speeds. As described in [4], the TWINS sensor does not report reliable wind speeds and directions below a wind speed of 2.8 m/s.

Extended Data Fig 3. Event S0235a waveform and polarisation summary. **a** shows VBB vertical time series indicating the picks associated to P and S phases. **b** and **c** show horizontal hodograms for P and S windows respectively. The time windows used to produce the hodograms are indicated by the grey shaded regions on **a**. The event back azimuth is indicated in the red dotted line in **b** and **c**, matching the first P-wave motion. A 2-5s bandpass filter is applied.

Extended Data Fig 4. Alignment of events with P-wave arrivals using vertical spectral envelopes. **a,** All events with P-wave energy aligned on a reference line; events are equally spaced sorted by distance; for each event we indicate the frequency band used to derive the spectral envelope and the amplification used in the display, so that all P waves have the same amplitude; glitches and the following S-wave are blanked out. **b,** P-wave envelopes overlapped for four of the events in the left panel; envelope amplitudes are re-scaled to show the similarity; S0173a and S0235b have clear P- and S-wave arrivals, while we observe only a strong first phase for S0183a and S0205a, interpreted as P-phase, and a weak second phase, interpreted as S-phase. The colour code of the events is the

same used in Fig 3. The spectral window length in **b** is 40 s to increase the visibility of the S-wave onsets.

Extended Data Fig 5. Alignment of events using their S-wave envelopes along a reference line. The top four events have significantly longer S-wave envelopes. S0183a and S0205a are not included as these events do not display a clearly visible S-wave. The colour code of the events is the same used in Fig 3.

Extended Data Table 1. List of events analysed in this paper. Event quality is as defined in the Methods section. The aligned distances follow Fig. 3, while the distance, back-azimuth and phase picks from the MQS catalogue are provided when available. The moment magnitude (M_W) is based on the spectral magnitude except for those events marked with an asterisk, that are derived from the 2.4Hz magnitude (Supplementary Information SI3).

Extended Data Table 2. SNR values for the events analysed in this paper. Frequency range used for computing the spectral envelopes are listed in the second and third columns. Four different SNR types computed using maxima and means of signal and noise, as well as maxima of P- and S envelopes are also given with the start and end times of the signal used. Events with little or no S-wave energy are also evident from the relative amplitude of SNRs (shaded cells).

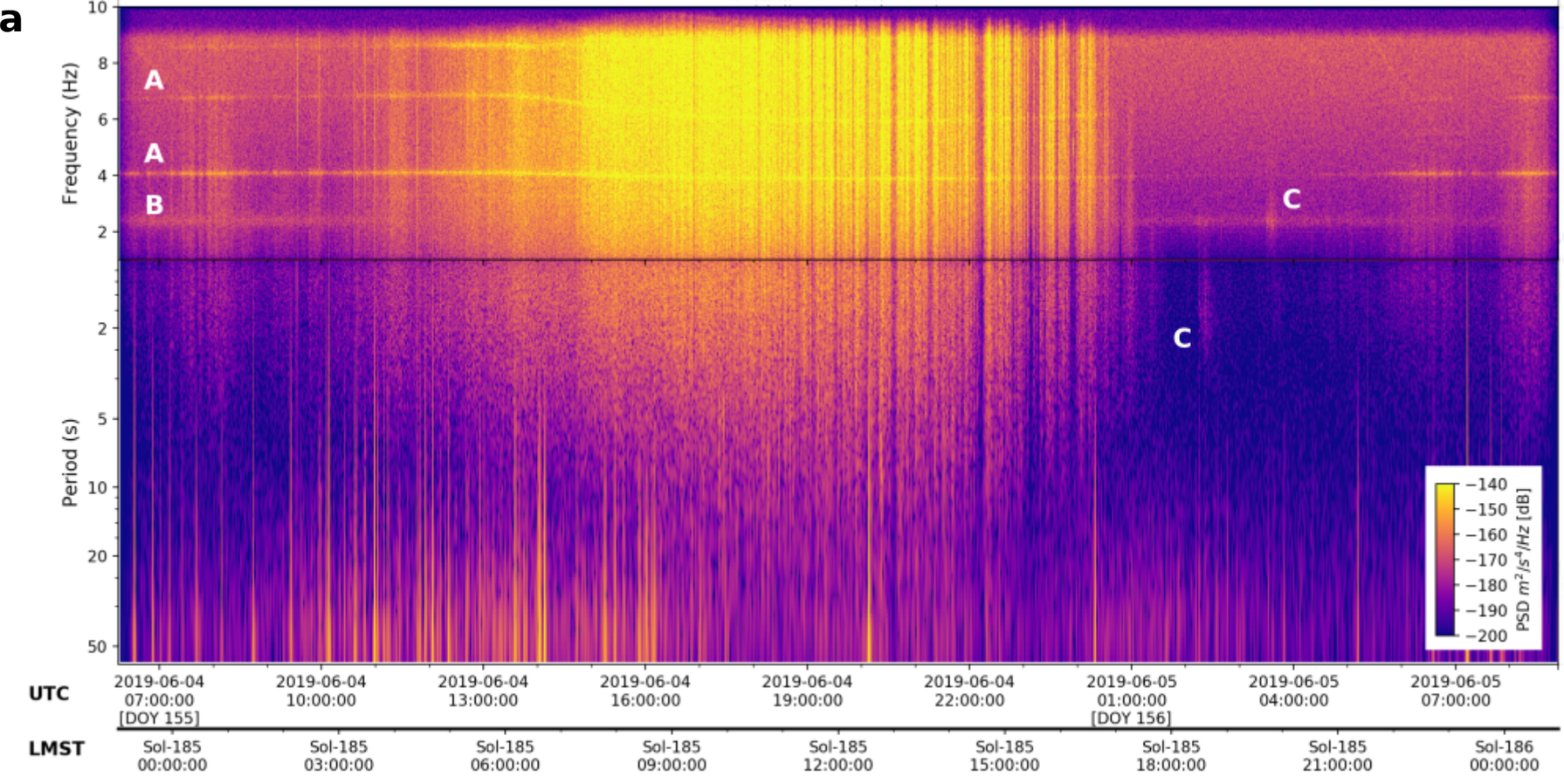
a
Frequency (Hz)
Period (s)
A
A
B
C
C
PSD $m^2/s^4/Hz$ [dB]
−140
−150
−160
−170
−180
−190
−200
UTC
2019-06-04 07:00:00 [DOY 155]
2019-06-04 10:00:00
2019-06-04 13:00:00
2019-06-04 16:00:00
2019-06-04 19:00:00
2019-06-04 22:00:00
2019-06-05 01:00:00 [DOY 156]
2019-06-05 04:00:00
2019-06-05 07:00:00
LMST
Sol-185 00:00:00
Sol-185 03:00:00
Sol-185 06:00:00
Sol-185 09:00:00
Sol-185 12:00:00
Sol-185 15:00:00
Sol-185 18:00:00
Sol-185 21:00:00
Sol-186 00:00:00

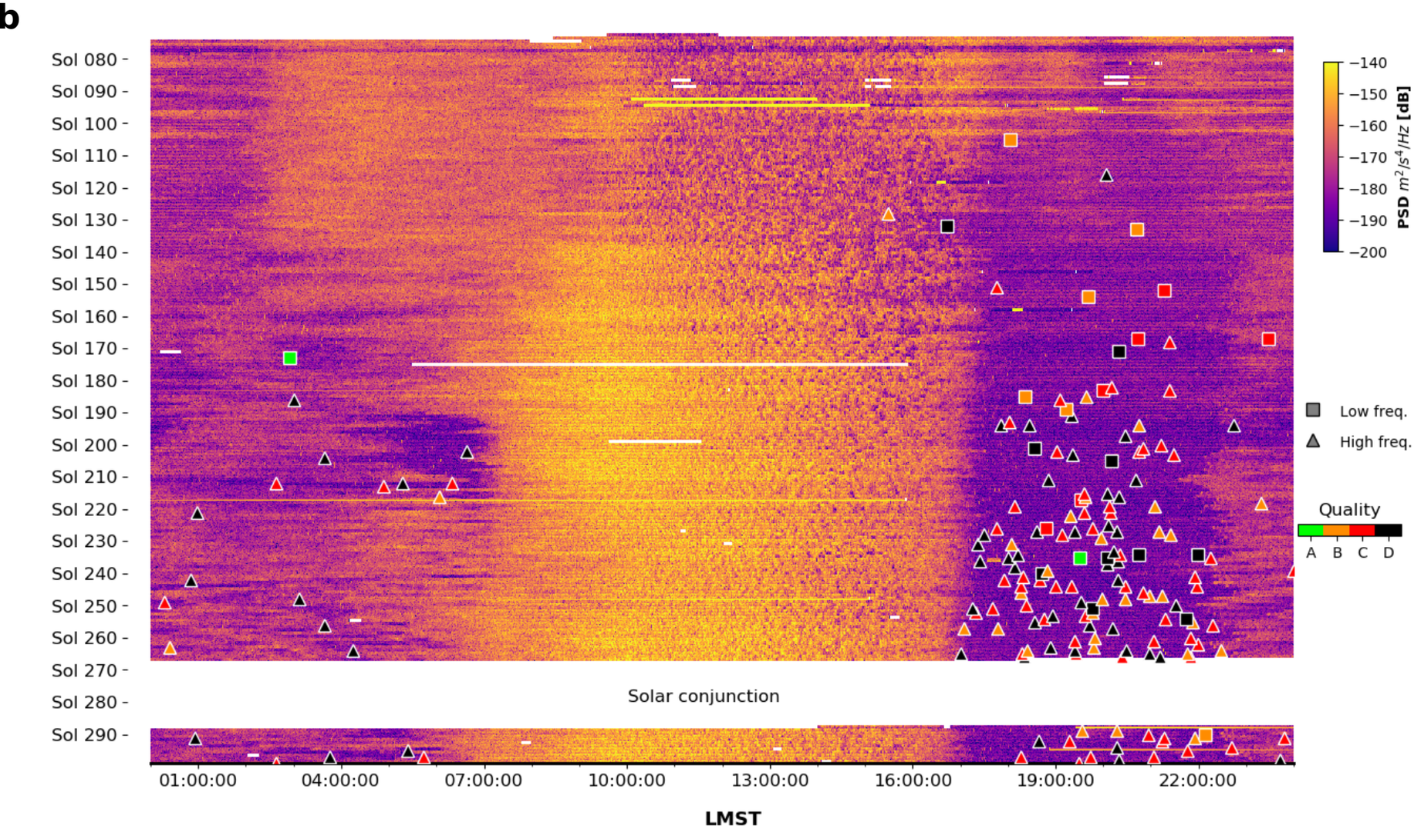
b
Sol 080
Sol 090
Sol 100
Sol 110
Sol 120
Sol 130
Sol 140
Sol 150
Sol 160
Sol 170
Sol 180
Sol 190
Sol 200
Sol 210
Sol 220
Sol 230
Sol 240
Sol 250
Sol 260
Sol 270
Sol 280
Sol 290
Solar conjunction
PSD $m^2/s^4/Hz$ [dB]
−140
−150
−160
−170
−180
−190
−200
Low freq.
High freq.
Quality
A B C D
01:00:00
04:00:00
07:00:00
10:00:00
13:00:00
16:00:00
19:00:00
22:00:00
LMST

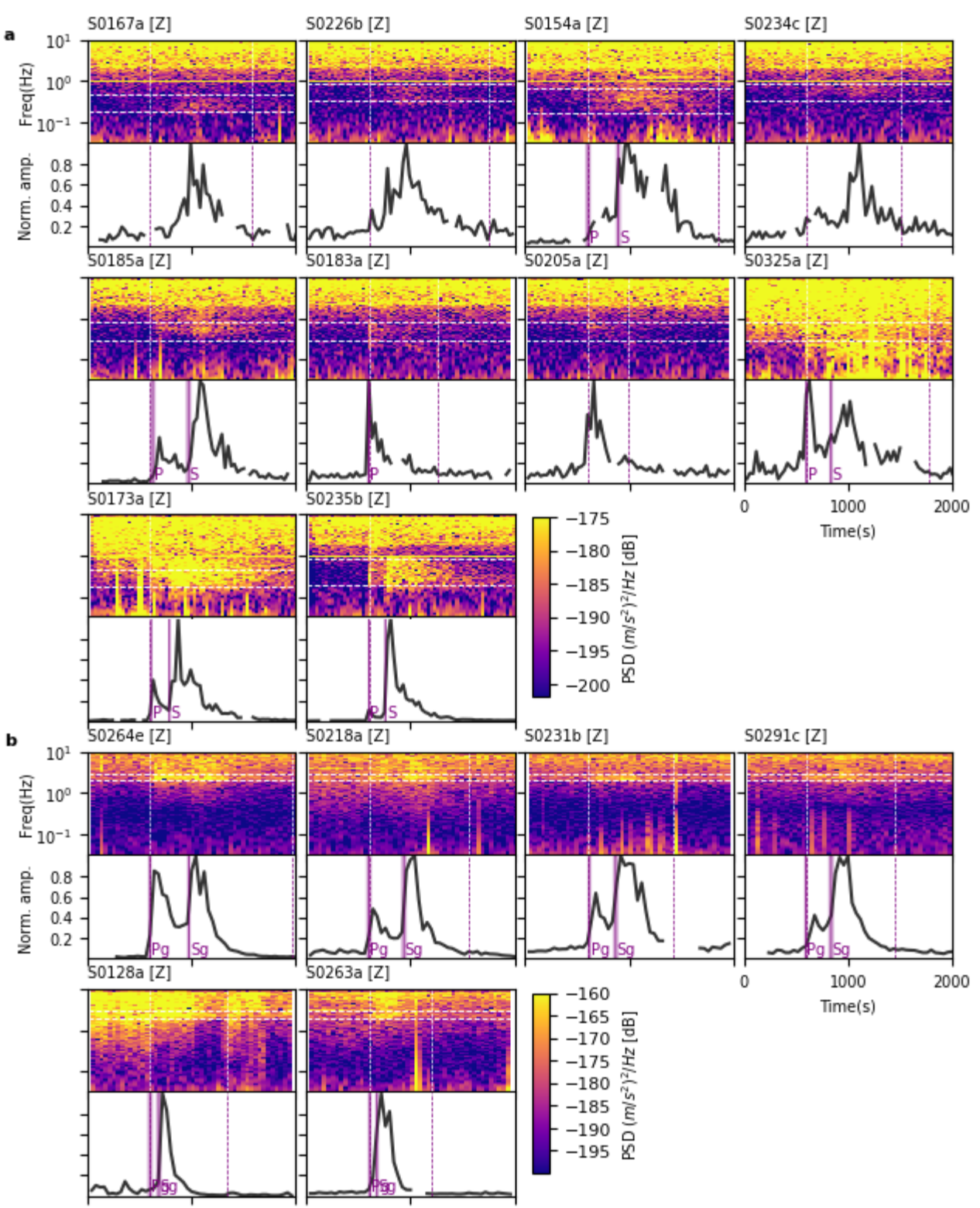
a
S0167a [Z]
S0226b [Z]
S0154a [Z]
S0234c [Z]
S0185a [Z]
S0183a [Z]
S0205a [Z]
S0325a [Z]
S0173a [Z]
S0235b [Z]
Freq(Hz)
Norm. amp.
P
S
Time(s)
PSD (m/s²)²/Hz [dB]
b
S0264e [Z]
S0218a [Z]
S0231b [Z]
S0291c [Z]
S0128a [Z]
S0263a [Z]
Pg
Sg

a

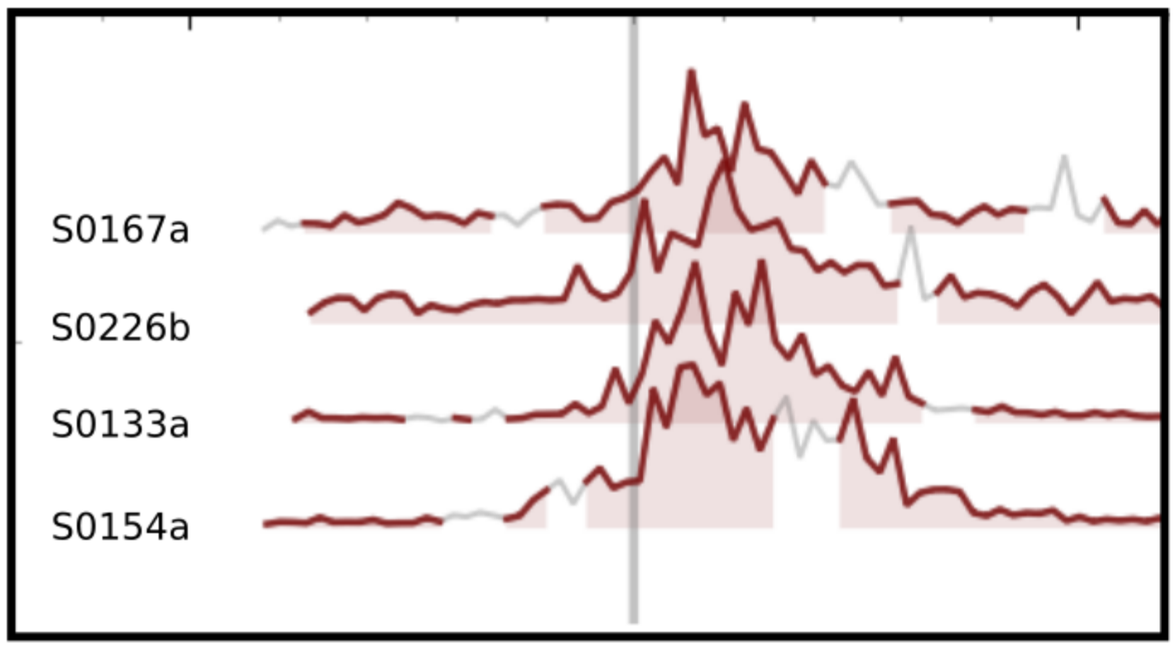
S0167a
S0226b
S0133a
S0154a

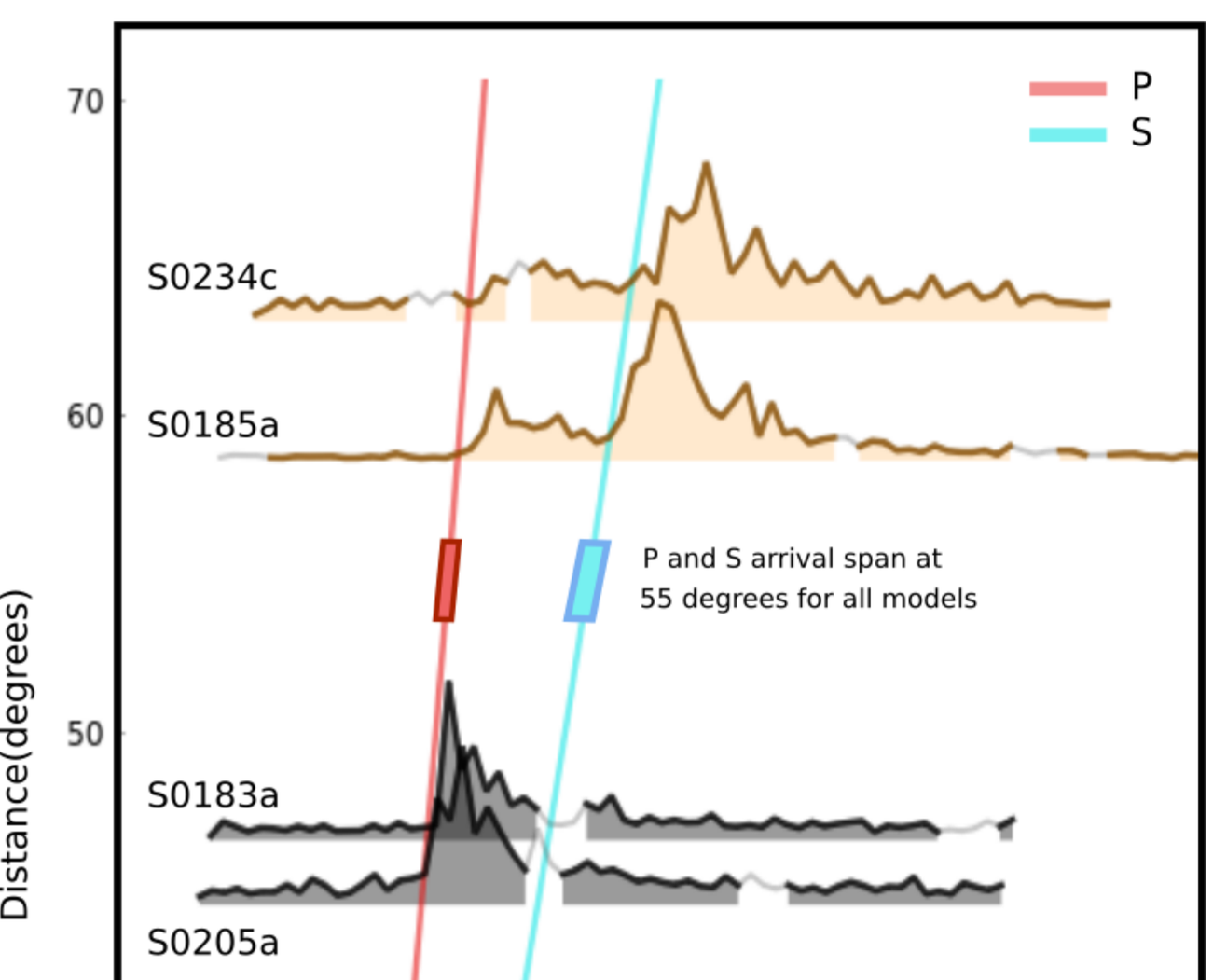
P
S
S0234c
S0185a
P and S arrival span at
55 degrees for all models
S0183a
S0205a
S0325a
S0173a
S0105a
S0189a
S0235b
70
60
50
40
30
20
Distance(degrees)
0
1000
2000
Time(s)

b

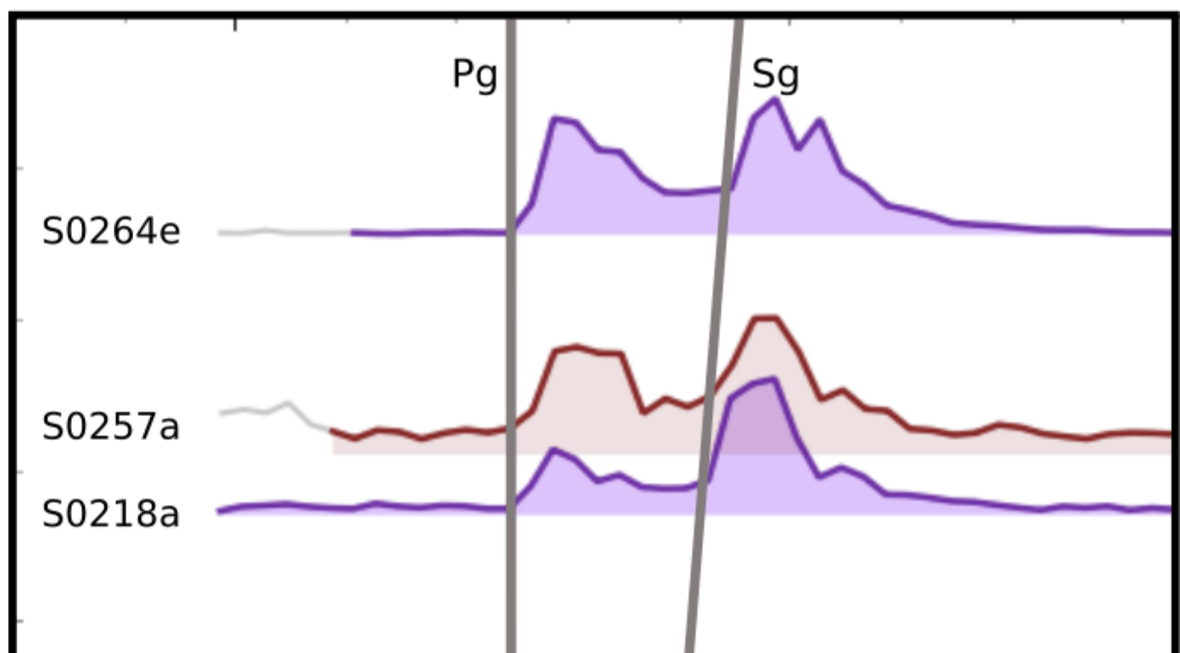
Pg
Sg
S0264e
S0257a
S0218a

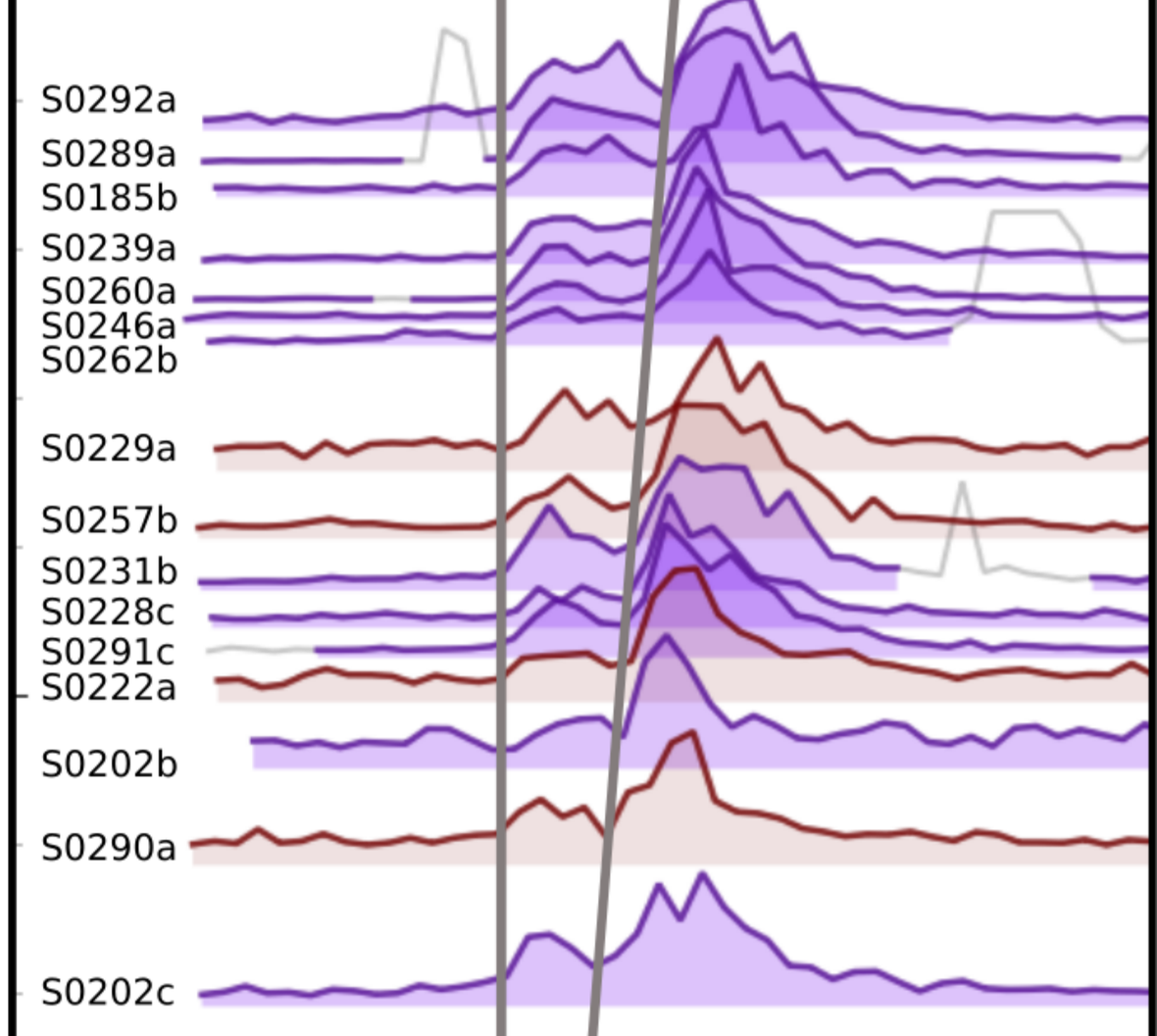
S0292a
S0289a
S0185b
S0239a
S0260a
S0246a
S0262b
S0229a
S0257b
S0231b
S0228c
S0291c
S0222a
S0202b
S0290a
S0202c
S0234b
S0226a
S0128a
S0263a
Distance
0
300
700
1100
Time after Pg (s)

a

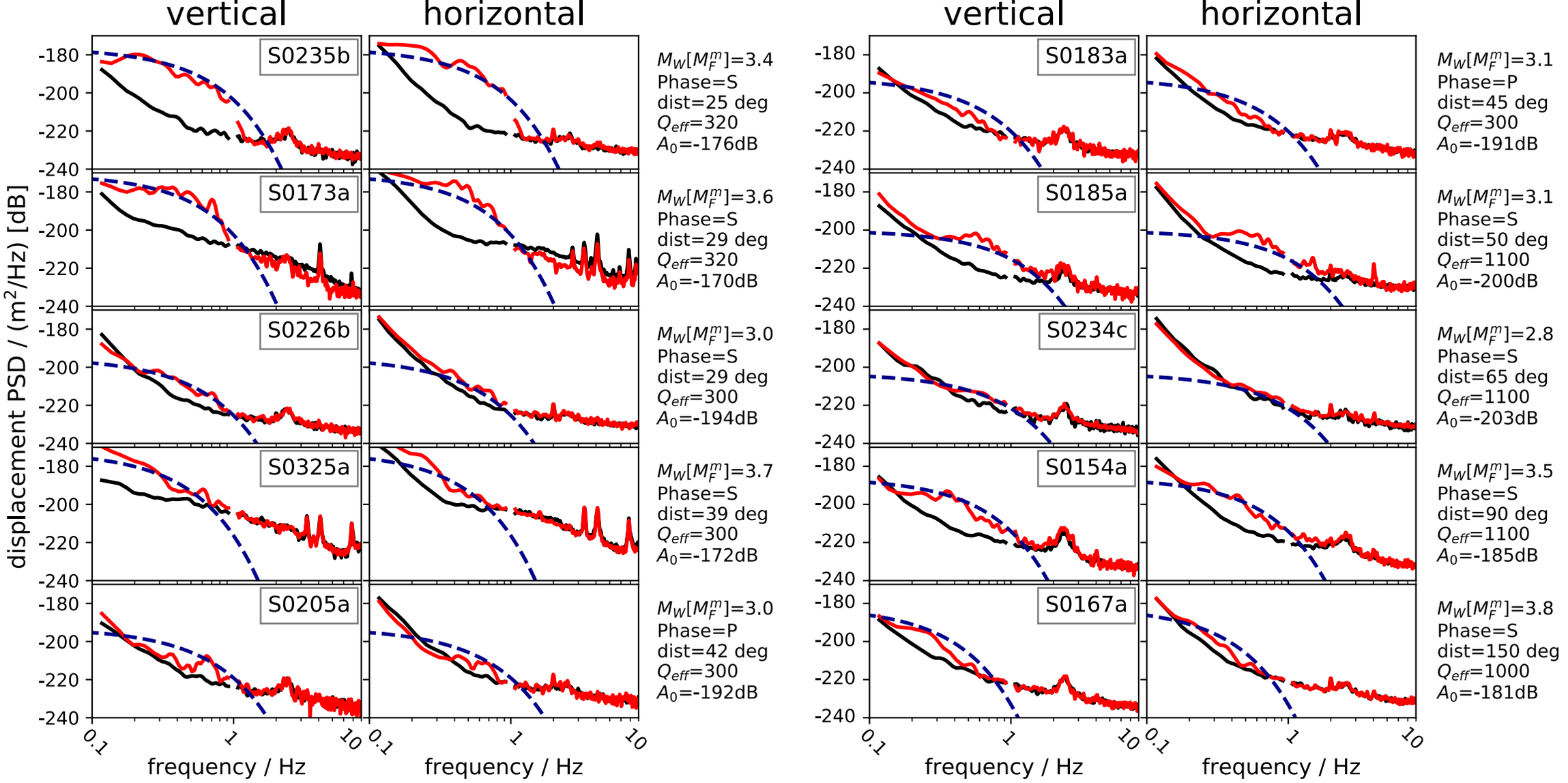
vertical
horizontal
vertical
horizontal
displacement PSD / (m²/Hz) [dB]
S0235b
S0173a
S0226b
S0325a
S0205a
S0183a
S0185a
S0234c
S0154a
S0167a
-180
-200
-220
-240
0.1
1
10
frequency / Hz
$M_W[M_F^m]$=3.4
Phase=S
dist=25 deg
Q_{eff}=320
A_0=-176dB
$M_W[M_F^m]$=3.6
Phase=S
dist=29 deg
Q_{eff}=320
A_0=-170dB
$M_W[M_F^m]$=3.0
Phase=S
dist=29 deg
Q_{eff}=300
A_0=-194dB
$M_W[M_F^m]$=3.7
Phase=S
dist=39 deg
Q_{eff}=300
A_0=-172dB
$M_W[M_F^m]$=3.0
Phase=P
dist=42 deg
Q_{eff}=300
A_0=-192dB
$M_W[M_F^m]$=3.1
Phase=P
dist=45 deg
Q_{eff}=300
A_0=-191dB
$M_W[M_F^m]$=3.1
Phase=S
dist=50 deg
Q_{eff}=1100
A_0=-200dB
$M_W[M_F^m]$=2.8
Phase=S
dist=65 deg
Q_{eff}=1100
A_0=-203dB
$M_W[M_F^m]$=3.5
Phase=S
dist=90 deg
Q_{eff}=1100
A_0=-185dB
$M_W[M_F^m]$=3.8
Phase=S
dist=150 deg
Q_{eff}=1000
A_0=-181dB

b

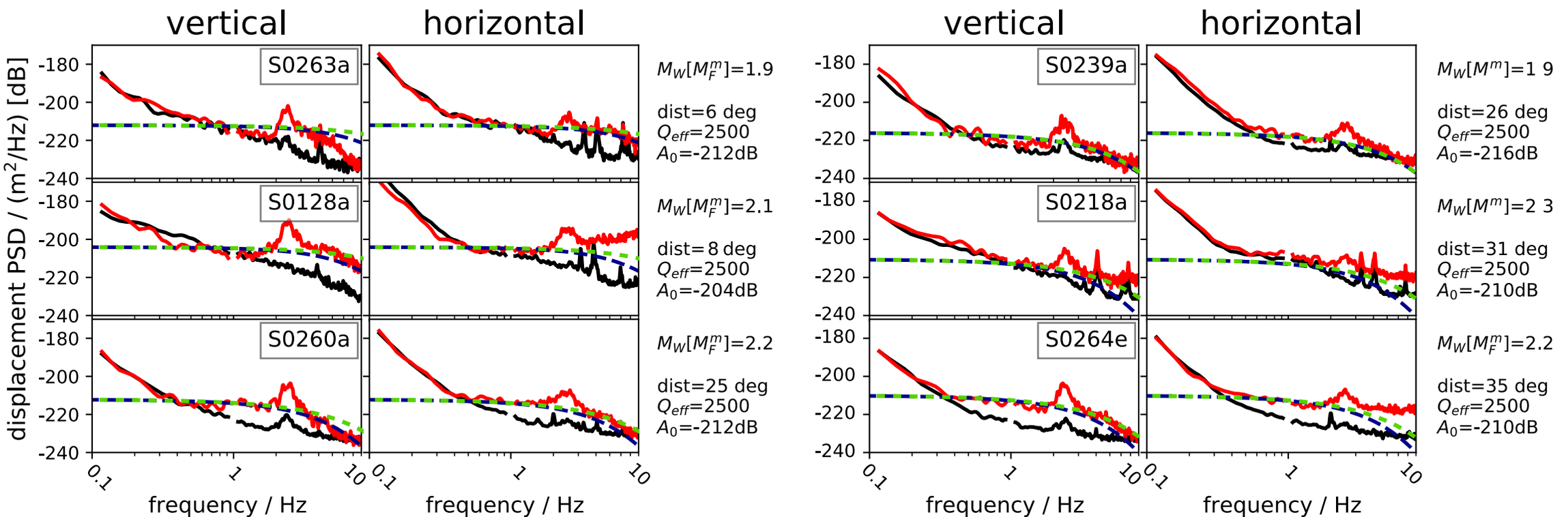
vertical
horizontal
vertical
horizontal
displacement PSD / (m²/Hz) [dB]
S0263a
S0128a
S0260a
S0239a
S0218a
S0264e
-180
-200
-220
-240
0.1
1
10
frequency / Hz
noise
event
Q only
Q & source
$M_W[M_F^m]$=1.9
dist=6 deg
Q_{eff}=2500
A_0=-212dB
$M_W[M_F^m]$=2.1
dist= 8 deg
Q_{eff}=2500
A_0=-204dB
$M_W[M_F^m]$=2.2
dist=25 deg
Q_{eff}=2500
A_0=-212dB
$M_W[M^m]$=1 9
dist=26 deg
Q_{eff}=2500
A_0=-216dB
$M_W[M^m]$=2 3
dist=31 deg
Q_{eff}=2500
A_0=-210dB
$M_W[M_F^m]$=2.2
dist=35 deg
Q_{eff}=2500
A_0=-210dB

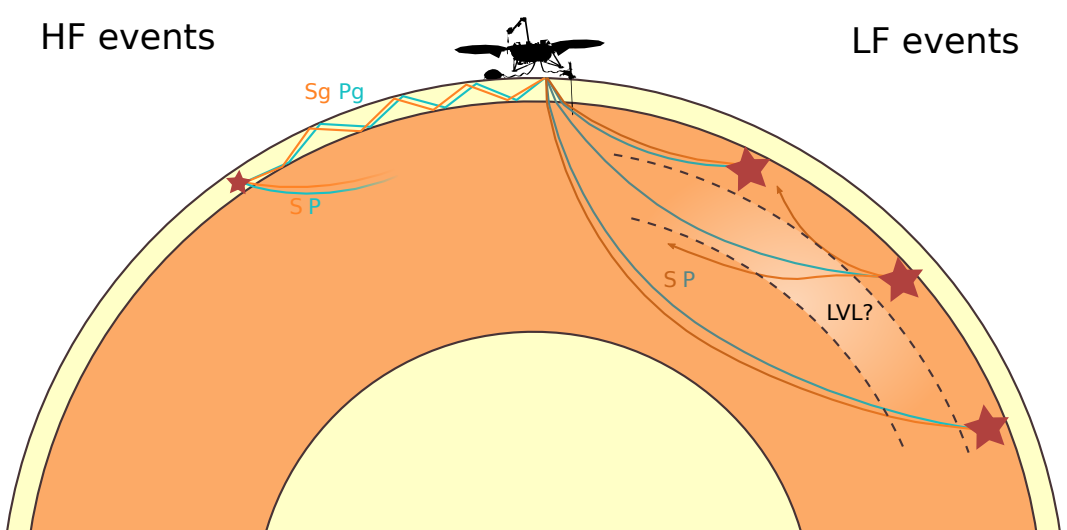
HF events
LF events
Sg Pg
S P
S P
LVL?

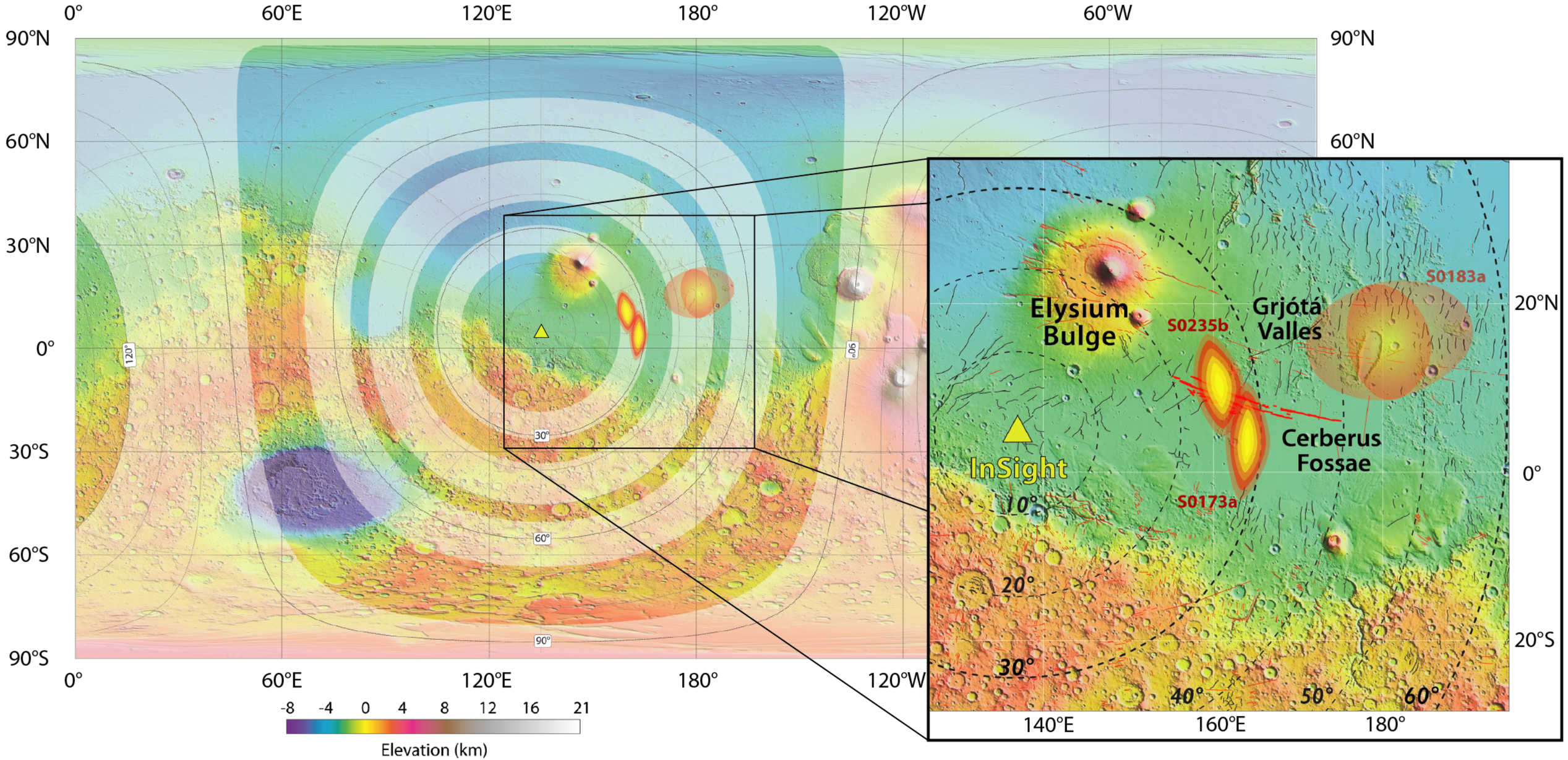
0°
60°E
120°E
180°
120°W
60°W
90°N
60°N
30°N
0°
30°S
60°S
90°S
120°
90°
60°
30°
-8 -4 0 4 8 12 16 21
Elevation (km)
Elysium Bulge
S0235b
S0183a
Grjótá Valles
Cerberus Fossae
S0173a
InSight
10°
20°
30°
40°
50°
60°
20°N
0°
20°S
140°E
160°E
180°

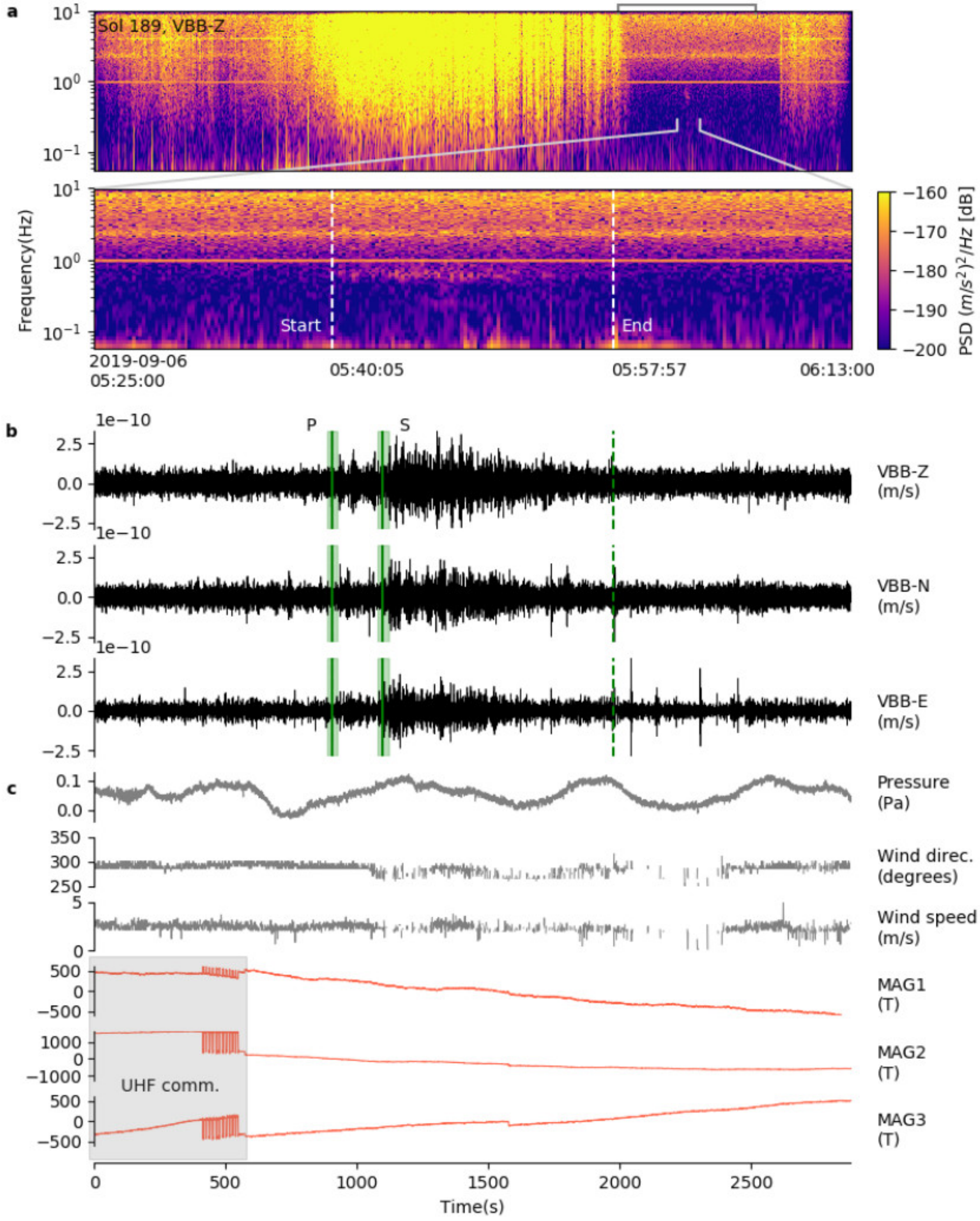
a
Sol 189, VBB-Z
Frequency(Hz)
Start
End
2019-09-06
05:25:00
05:40:05
05:57:57
06:13:00
PSD (m/s²)²/Hz [dB]
b
P
S
VBB-Z
(m/s)
VBB-N
(m/s)
VBB-E
(m/s)
c
Pressure
(Pa)
Wind direc.
(degrees)
Wind speed
(m/s)
MAG1
(T)
MAG2
(T)
MAG3
(T)
UHF comm.
Time(s)

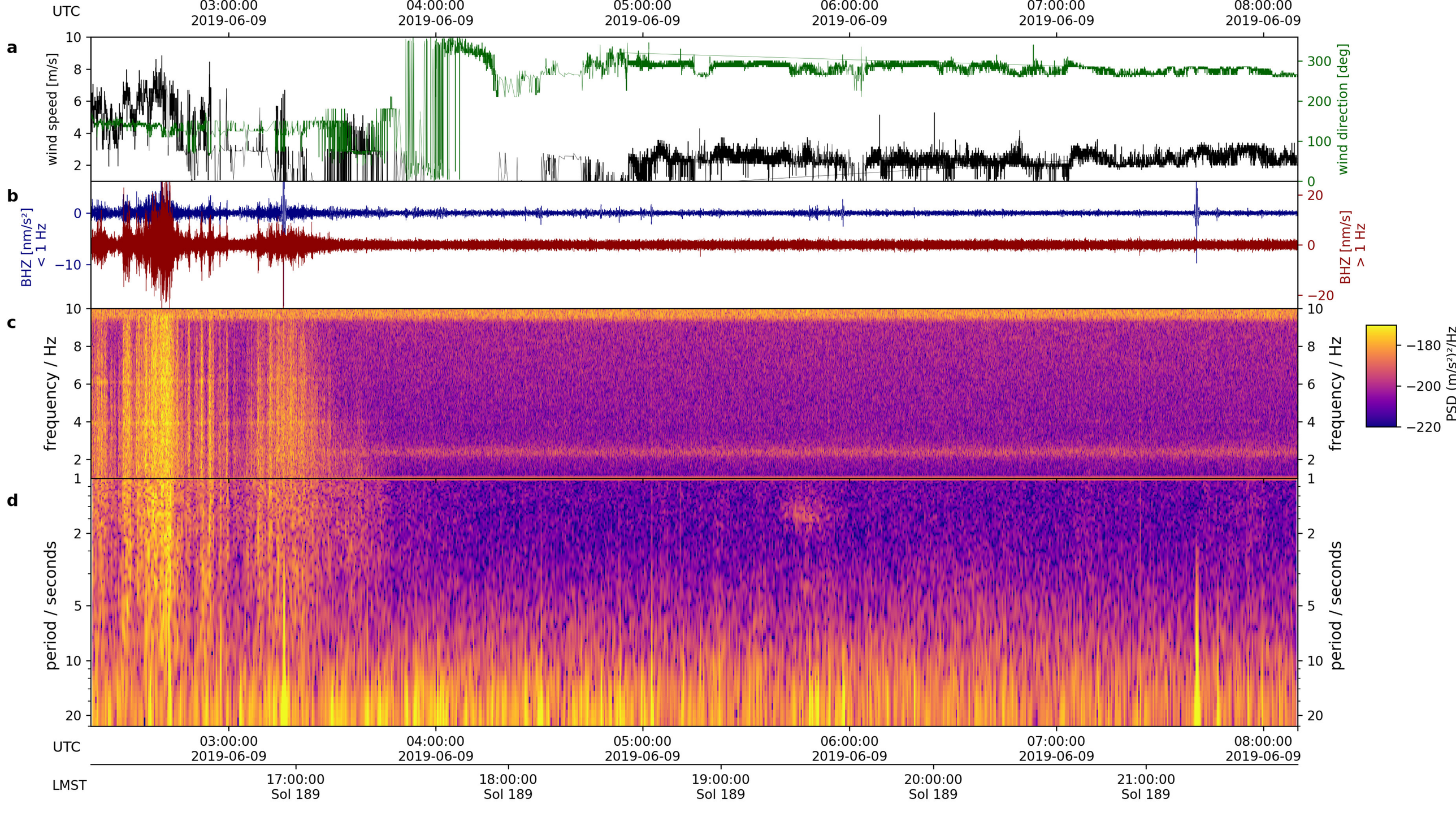
UTC
03:00:00
2019-06-09
04:00:00
2019-06-09
05:00:00
2019-06-09
06:00:00
2019-06-09
07:00:00
2019-06-09
08:00:00
2019-06-09
a
wind speed [m/s]
wind direction [deg]
b
BHZ [nm/s²]
< 1 Hz
BHZ [nm/s]
> 1 Hz
c
frequency / Hz
PSD (m/s²)²/Hz
d
period / seconds
UTC
LMST
17:00:00
Sol 189
18:00:00
Sol 189
19:00:00
Sol 189
20:00:00
Sol 189
21:00:00
Sol 189

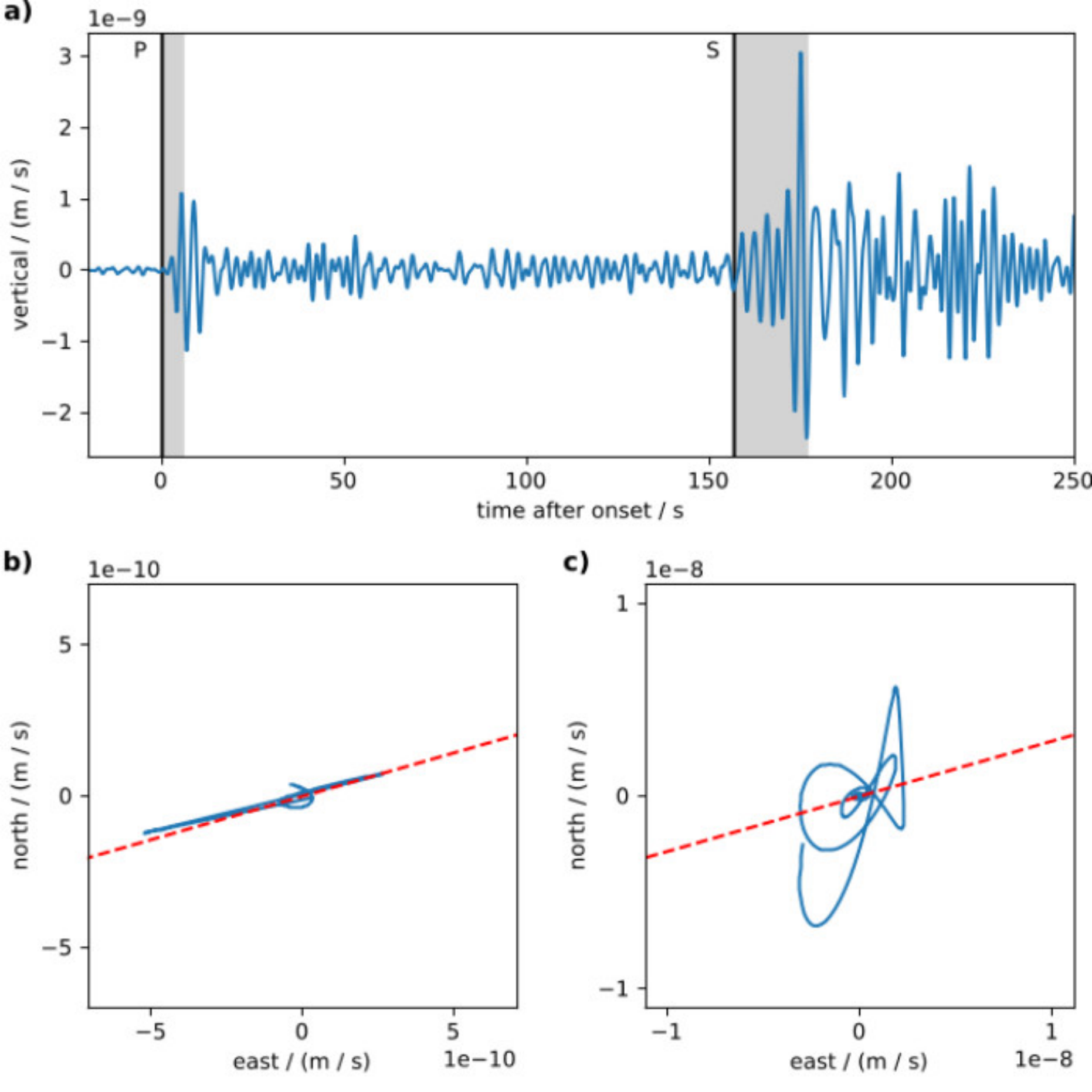
a)
1e−9
P
S
vertical / (m / s)
time after onset / s
b)
1e−10
north / (m / s)
east / (m / s)
1e−10
c)
1e−8
north / (m / s)
east / (m / s)
1e−8

Vertical component

a

S0234c
(0.33-0.83Hz, 132x)

S0185a
(0.33-0.83Hz, 1530x)

S0183a
(0.33-0.67Hz, 270x)

S0205a
(0.28-0.83Hz, 860x)

S0325a
(0.20-0.80Hz, 745x)

S0173a
(0.20-0.67Hz, 44x)

S0105a
(0.30-0.50Hz, 2560x)

S0189a
(0.36-0.83Hz, 860x)

S0235b
(0.15-0.90Hz, 270x)

0 300 600

Time after P-envelope (s)

b

S0235b
S0173a
S0325a
S0183a
S0205a

Start of S-wave envelope

S0183a, S0205a
S0173a, S0235b
S0325a

Start of P-wave envelope

0 200 400

Time after P-envelope (s)

Vertical

North

East

S0167a
(0.18-0.48Hz, 660x

S0226b
(0.33-0.83Hz, 1287x

S0133a
(0.33-0.83Hz, 766x

S0154a
(0.17-0.67Hz, 716x

S0234c
(0.33-0.83Hz, 90x

S0185a
(0.30-0.83Hz, 90x

S0173a
(0.20-0.50Hz, 44x

S0105a
(0.3-0.50Hz, 1529x

S0189a
(0.35-0.83Hz, 623x

S0235b
(0.15-0.90Hz, 55x

0 1000

0 1000

0 1000

Time after S-envelope start (s)

Event name	Event quality	Aligned distance (◦)	Catalogue distance (◦)	Catalogue back-azimuth (◦)	P pick (s) *Time (uncertainty)*	S pick (s) *Time (uncertainty)*	Magnitude M_W
Low Frequency events							
S0105a	B	27 (±5)	31 (±10)		2019-03-14 21:03:31 (±20)	2019-03-14 21:06:39 (±20)	3.2
S0133a	B	[90] (±20)	33 (±7)		2019-04-12 18:14:35 (±60)	2019-04-12 18:17:56 (±20)	3.2
S0154a	B	[90] (±20)	49 (±7)		2019-05-04 07:07:05 (±20)	2019-05-04 07:11:57 (±20)	3.5
S0167a	C	[150] (±20)					3.8
S0173a	A	28 (±3)	29 (±3)	91 (±5)	2019-05-23 02:22:59.1 (±1)	2019-05-23 02:25:53.8 (±2)	3.6
S0183a	C	47 (±10)		73 (±20)	2019-06-03 02:27:45.8 (±1)	2019-06-03 02:32:09 (±10)	3.1
S0185a	B	60 (±3)	59 (±10)		2019-06-05 02:13:51 (±20)	2019-06-05 02:19:35 (±20)	3.1
S0189a	B	27 (±5)	32 (±7)		2019-06-09 05:40:06 (±20)	2019-06-09 05:43:20 (±20)	3.0
S0205a	D	[45] (±10)					3.0
S0226b	C	[90] (±20)					
S0234c	D	65 (±5)					2.8
S0235b	A	25 (±3)	26 (±3)	74 (±15)	2019-07-26 12:19:19.3 (±2)	2019-07-26 12:21:56.1 (±2)	3.6
S0325a	B	35 (±5)	40 (±5)		2019-10-26 06:58:58.9 (±1)	2019-10-26 07:02:56 (±10)	3.7

			P_g pick (s)	S_g pick (s)	
High Frequency events					
S0128a	B	8	2019-04-07 09:33:36 (±20)	2019-04-07 09:35:00 (±20)	2.1
S0185b	B	31	2019-06-05 03:29:16 (±10)	2019-06-05 03:34:12 (±10)	2.0
S0202b	C	14	2019-06-22 14:01:35 (±20)	2019-06-22 14:04:08 (±20)	1.8
S0202c	C	24	2019-06-22 15:49:43 (±20)	2019-06-22 15:54:00 (±20)	1.9
S0218a	B	32	2019-07-09 05:03:01 (±20)	2019-07-09 05:08:37 (±20)	2.3
S0222a	B	20	2019-07-13 03:32:40 (±10)	2019-07-13 03:36:17 (±20)	1.6*
S0226a	C	9	2019-07-17 04:33:03 (±20)	2019-07-17 04:34:40 (±20)	1.5
S0228c	B	22	2019-07-19 09:38:29 (±10)	2019-07-19 09:42:21 (±20)	1.9
S0229a	B	26	2019-07-20 08:50:24 (±20)	2019-07-20 08:55:05 (±20)	1.6*
S0231b	B	24	2019-07-22 08:10:11 (±10)	2019-07-22 08:14:24 (±20)	1.9
S0234b	C	13	2019-07-25 12:35:15 (±20)	2019-07-25 12:37:37 (±20)	1.3*
S0239a	B	27	2019-07-30 14:17:03 (±10)	2019-07-30 14:21:49 (±10)	1.9
S0246a	B	26	2019-08-06 18:16:36 (±20)	2019-08-06 18:21:12 (±20)	1.8
S0257a	B	31	2019-08-18 00:23:06 (±20)	2019-08-18 00:28:34 (±20)	1.8*
S0257b	B	26	2019-08-18 01:05:46 (±10)	2019-08-18 01:10:26 (±20)	1.7*
S0260a	B	26	2019-08-21 05:11:21 (±10)	2019-08-21 05:15:55 (±20)	2.2
S0262b	C	25	2019-08-23 08:39:53 (±10)	2019-08-23 08:44:18 (±20)	2.2
S0263a	B	7	2019-08-23 11:09:54 (±10)	2019-08-23 11:11:04 (±10)	1.9
S0264e	B	35	2019-08-25 10:31:35 (±10)	2019-08-25 10:37:48 (±10)	2.2
S0289a	B	27	2019-09-20 00:02:04 (±20)	2019-09-20 00:06:49 (±20)	2.3
S0290a	C	22	2019-09-21 02:06:12 (±20)	2019-09-21 02:10:10 (±20)	1.6*
S0291c	B	23	2019-09-22 03:46:08 (±10)	2019-09-22 03:50:11 (±20)	2.0
S0292a	C	32	2019-09-23 03:46:08 (±20)	2019-09-23 03:51:48 (±20)	1.9

* M_W magnitudes are derived from the spectral magnitude ($M_{\mathrm{FB}}^{\mathrm{Ma}}$), except for those indicated with * which are based on the 2.4Hz magnitude ($M_{2.4\mathrm{Hz}}^{\mathrm{Ma}}$)

			SNRs from spectral envelopes					
Event name	f_{min}	f_{max}	Peak signal/ peak noise	Mean signal/ mean noise	max(P)/max(noise)	max(S)/max(noise)	Signal start	Signal end
Low frequency								
S0105a	0.31	0.5	7.8	6.1	4.7	7.8	2019-03-14 20:53:28	2019-03-14 21:28:57
S0133a	0.33	0.67	10.5	6.5	6.3	10.5	2019-04-12 18:04:34	2019-04-12 18:38:48
S0154a	0.17	0.67	7.7	6.8	6.9	7.7	2019-05-04 6:57:00	2019-05-04 7:37:48
S0167a	0.18	0.47	4.9	2.8	3.6	4.9	2019-05-17 16:37:15	2019-05-17 17:13:27
S0173a	0.18	0.67	95	16.9	19	95	2019-05-23 2:12:48	2019-05-23 3:10:23
S0183a	0.3	0.8	5.3	2.8	5.3	1.7	2019-06-03 2:17:47	2019-06-03 3:01:07
S0185a	0.29	0.83	14.1	5.4	5.2	14.1	2019-06-05 2:03:25	2019-06-05 2:49:55
S0189a	0.36	0.83	10.6	5.1	5	10.6	2019-06-09 5:30:05	2019-06-09 6:07:57
S0205a	0.3	0.8	4.8	3.8	4.8		2019-06-25 16:59:43	2019-06-25 17:43:03
S0226b	0.33	0.83	5.1	2.5	2.3	5.1	2019-07-17 5:33:38	2019-07-17 6:12:49
S0234c	0.33	0.83	3.8	2.4	2.4	3.8	2019-07-25 12:44:18	2019-07-25 13:19:32
S0235b	0.2	0.85	251.7	25.2	31	251.7	2019-07-26 12:09:16	2019-07-26 13:28:08
S0325a	0.3	0.8	3.5	2.9	3.5	3.2	2019-10-26 6:48:58	2019-10-26 7:28:35
High-frequency								
S0128a	2	3	7.2	3.2	1	7.2	2019-04-07 9:23:36	2019-04-07 10:06:56
S0185b	2	3	10.8	3.9	3.7	10.8	2019-06-05 3:19:15	2019-06-05 3:55:25
S0202b	2	3	3	1.6	1.2	3	2019-06-22 13:51:40	2019-06-22 14:35:00
S0202c	2	3	5.5	2.9	2.3	5.5	2019-06-22 15:40:25	2019-06-22 16:17:28
S0218a	2	3	11.6	5.1	5.3	11.6	2019-07-09 4:53:00	2019-07-09 5:28:53
S0222a	2	3	3.5	2.4	1.4	3.5	2019-07-13 3:22:44	2019-07-13 4:06:04
S0226a	2	3	3.1	2.2	1.2	3.1	2019-07-17 4:23:02	2019-07-17 5:06:22
S0228c	2	3	7.5	3.6	3	7.5	2019-07-19 9:28:15	2019-07-19 10:02:21
S0229a	2	3	3.9	2.2	3.1	3.9	2019-07-20 8:40:08	2019-07-20 9:14:03
S0231b	2	3	6.9	4.8	2.8	6.9	2019-07-22 7:59:53	2019-07-22 8:33:42
S0234b	2	3	1.5	1.2	1.3	1.5	2019-07-25 12:25:08	2019-07-25 13:08:28
S0239a	2	3	11.5	5	7.2	11.5	2019-07-30 14:06:49	2019-07-30 14:42:10
S0246a	2	3	7.4	4.1	2.5	7.4	2019-08-06 18:05:50	2019-08-06 18:42:02
S0257a	2	3	5	3.2	4.7	5	2019-08-18 0:13:04	2019-08-18 0:46:46
S0257b	2	3	6.8	4.6	2.8	6.8	2019-08-18 0:55:34	2019-08-18 1:38:54
S0260a	2	3	38.3	15.6	17	38.3	2019-08-21 5:01:08	2019-08-21 5:38:41
S0262b	2	3	5.5	2.5	1.2	5.5	2019-08-23 8:29:46	2019-08-23 9:00:34
S0263a	2	3	17.4	13.2	1.4	17.4	2019-08-23 10:59:44	2019-08-23 11:43:04
S0264e	2	3	47.9	21	44.8	47.9	2019-08-25 10:21:36	2019-08-25 11:04:18
S0289a	2	3	18.1	9.9	6.7	18.1	2019-09-19 23:51:50	2019-09-20 0:27:52
S0290a	2	3	3.5	1.8	1.7	3.5	2019-09-21 1:56:14	2019-09-21 2:30:56
S0291c	2	3	11.1	5.9	3.8	11.1	2019-09-22 3:36:12	2019-09-22 4:10:24
S0292a	2	3	8	4.3	4.3	8	2019-09-23 3:34:42	2019-09-23 4:11:48

SI1. Wind noise and Signal to Noise (SNR) for events

Noise characteristics

All low frequency events, with the exception of events S105a, S0173a, S0167b and S0235b have amplitudes below 10^{-9} m/s^2/Hz$^{1/2}$ and moreover several events have maximum spectral amplitude less than 3×10^{-10} m/s^2/Hz$^{1/2}$. As shown and developed in Lognonné et al., this volume, these amplitudes are comparable to the wind induced lander noise. A careful noise analysis is therefore required for assessing the possible wind corruption.

The first source of noise between 0.1 and 1Hz is likely related to lander vibrations, though not resonances. While on the deck, prior to surface deployment, the SEIS-SP instrument recorded accelerations in this bandwidth between 5×10^{-8} and 10^{-5} m/s^2/Hz$^{1/2}$ depending on the wind and local time. These vibrations are transferred to the ground through the feet of the lander as an inertial force, producing a static deformation of the regolith and its crust, in addition to possible coupling though the tether (Murdoch et al., 2017a). Additionally, glitches provide a second source of noise in this bandwidth, owing to thermal and wind induced tilts (Lognonné et al., this volume).

The InSight TWINS wind sensors (Banfield et al., 2019) are unable to provide precise data in the same bandwidth as SEIS and have limited to no resolution for low wind. For winds below 0.7 m/s to 1.8 m/s and corresponding to Reynolds number smaller than 50, the resolution is unknown and so the data are unreliable. For a Reynolds number up to 90 (corresponding to wind speed up to 2.8 m/s for a pressure of 750 Pa), the full resolution of 0.4 m/s might in addition not be reached (Banfield et al, this volume).

Most wind data are acquired at a rate of 1 measurement every 2 seconds with the addition of some periods obtained at a rate of 1 measurement per second. No wind data are therefore available in the frequency bandwidth of the recorded events, above 0.2 Hz. Both long period and short period observations shows however a significant wind sensitivity, which is detailed in Lognonné et al., this volume, Supplementary Information SI1 and shows a clear increase of the noise with the mean wind.

Vertical noise levels and associated fluctuations are shown in Figure SI1.1, which shows the wind levels obtained for different periods and, for a squared wind of 10.5 (m/s)^2, the variability of all spectra. This suggest a variability of ±50% of the amplitude at 1-sigma, and therefore a power spectrum SNR with respect to this source of noise of 2.25 in order to be above the 1-

sigma level. Note that this variability can also lead to wind noise smaller than the average by a factor of about 2.

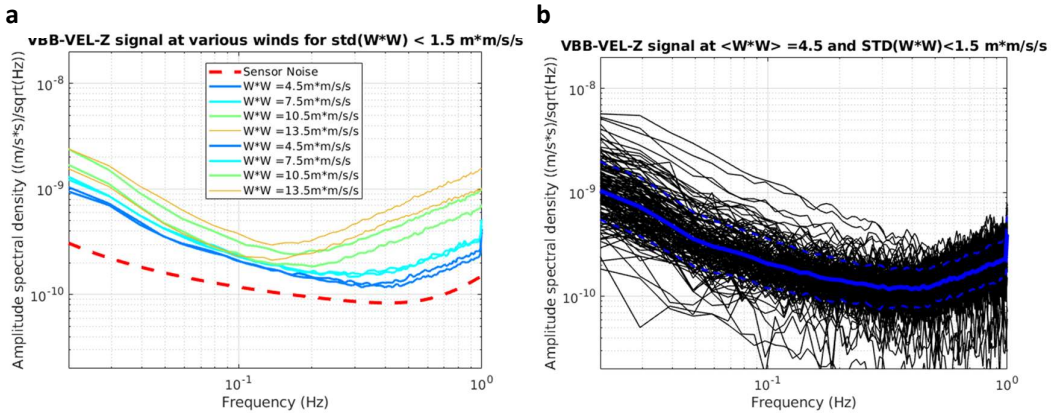

Figure SI1.1. **a**, Z axis noise for low winds (up to ~3.7 m/s = 13.5 $(m/s)^2$ and standard deviation of wind-squared speed lower than 1.5 $(m/s)^2$) estimated from two sol ranges: 168-174 and 176-182. **b,** SEIS-VBBZ noise fluctuations for spectrum of 161 windows of 400 second-long in the 176-182 sols range, all taken for a same set of wind-squared (in the 3 to 6 $(m/s)^2$ range) and wind-squared standard-deviation (in the 0-1.5 $(m/s)^2$).

A priori SNR from wind data

A proposed approach is to define a SNR with respect to the wind by analyzing the variations of the SEIS axis noise, as a function of the mean squared wind. We used the noise shown in Figure SI2.1 (from Lognonné et al, this volume) to express the statistical noise level and limit the discussion to the Z axis of the VBB instrument. This noise model is approximated by the following expression for the power spectral amplitude n^2:

$$n^2 = e^2 + \left(0.0058\ \frac{<v^2>}{f^2} + 0.44 f^2 < v^2 >^2\right) 10^{-20} ms^{-2} Hz^{-1/2},$$

where $<v^2>$ is the mean squared wind in $(m/s)^2$ over a given time window, f the frequency in Hz and e the VBB self-noise power for no wind. The self-noise is about 50% of the noise level for a mean squared wind of 4.5 $(m/s)^2$. This expression fits to the observed noise at level better than 30% for winds up to 4 m/s, which is comparable to the noise levels observed for different sols (see Figure SI1.1).

We use this wind noise to compute the a priori wind SNR, named SNRZW. It will be used to provide an initial assessment of the potential corruption of the event by wind. For an event in

which energy is mostly detected between two frequencies f_1 and f_2, the SNR is then simply defined as the ratio of the event's integrated PSD by the integrated energy of the above model, both integrations being done between f_1 and f_2. This is practically done by using the TWINS data for computing the mean squared wind in the time window of the event. In order to address the limitation of TWINS described above for winds lower than 1.8 m/s, we use a worst-case approach and assign to all TWINS value lower than 1.8 m/s the worst-case value of 1.8 m/s. The variability of the wind is characterized by computing the maximum wind in the event window.

For events S0105, S0133a, S0154a, S0167a, S0183a, S0185a, S0189a, the average wind is intermediate and ranging from 2.0 to 2.8 m/s in the event time window, while for event S0173a, the mean wind is larger than 3.25 m/s. Wind peaks range from 3.4 to 4 m/s for all events, except S0183a, for which the maximum wind burst is 4.4 m/s. For events S0226b, S0234c, S0235b, the mean wind low and below the 1.8 m/s limit, while the peaks range from 2.1 to 2.4 m/s, and TWINs is likely unable to resolve these low winds and only the seismic SNR shall be considered. Figure SI1.2 shows all individual spectra for these LP-BB events for these three wind conditions while the SNR are given in Table SI1.1.

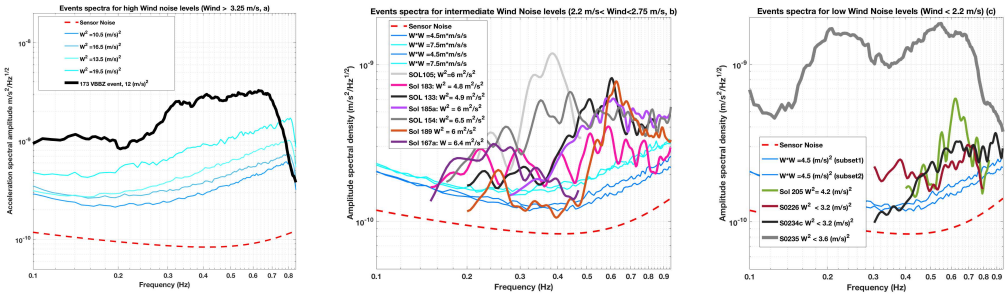

Figure SI1.2: Comparison of the events spectra with the a priori wind level for all LP and BB events and for 3 different wind regimes. (a) Events S0173a as compared to noise levels with wind > 3.25 m/s (b) Events S0105a, S0133a, S0154a, S0167a, S0185a, S0189a for noise levels with wind between 2.2 m/s and 2.75 m/s, (c) S0205a, S0226b, S0234c and S0235b for the a priori low noise levels with winds < 2.2 m/s. For each event, the square of the mean wind in the time window used for the spectrum computation is given. The thin blue lines are the mean noise levels found for the two time windows provided in Table SI1.2.

SNR from seismic only analysis (peak-to-peak and mean)

We compute SNRs from seismic data using two approaches:

1) We use the spectral characteristics of the signal and the noise, for a direct comparison with the wind a priori: We define the spectral SNR as the ratio of spectral power during the event compared to pre-event noise spectral power. The spectral power is calculated by integrating over the power spectral density in the same frequency range described in Table SI1.1. The power spectral density is estimated using Welch's method on 50s long time windows with an overlap of 50%, separately detrended and tapered with a Hanning window. The data has been corrected for the instrument response, converted to acceleration and rotated to a ZNE coordinate system. Event windows are the same as for the a priori wind and noise windows and are available in the MQS catalogue. Results are provided in Table SI1.1 for a selection of low frequency (LF) and high frequency (HF) events for the purpose of wind contamination analysis, using a spectral window length of 40 s. The SNRs for the full list of events are in Extended Data Table 2.

2) We also estimate SNR values on the spectral envelopes (SEs). The SEs are computed on acceleration spectrograms for the frequency band specific to each event, using the window lengths of 40s and 60s with an overlap of 50% after instrument correction and rotation to ZNE orientation. Next, we visually check spectrograms and mask the envelope time series where there is apparent contamination from glitches (Fig. 3 in the main text). These masked portions are ignored in any analysis done using the envelopes.

We provide four measures of SNRs using envelopes: a) Amplitude ratios of maxima (peak-to-peak SNR), b) mean (mean-to-mean SNR) of signal and noise, c) P-wave envelopes SNR, and d) S-wave envelopes SNR. Maximum energy for S0183a and for S0234c is within the P-wave windows; hence, peak-to-peak and P-window SNR values for these events are equal. Similarly, all other events have same SNR values for S-wave and peak-to-peak amplitudes, as maximum energy already lies inside the S-wave window. Table SI1.2 lists related SDE amplitudes as well as the frequency bands that SNR values and SDEs are computed.

SNR from moment matching of signal energies

While the pressure and wind signals are not found to be coherent to the seismic signal to any substantial degree in the seismic bandwidth, the pressure and seismic energies are found to co-modulate with the wind speed, though with a time-dependent sensitivity (Lognonné et al., this

issue, Supplementary Information 1). We use a time-dependent sensitivity from the variation of pressure energy and wind speed with seismic energy prior to an event, and hence estimate the environmental injection during the event. This is achieved by calculating the first and second moments, the mean and variance, of the pressure energy, wind speed and seismic energy within a window, and then recalculating the subsequent pressure and wind time series to match the mean and variance of the seismic time series in the window. Essentially the gain and offset of the two time series are adjusted to best match the seismic time series.

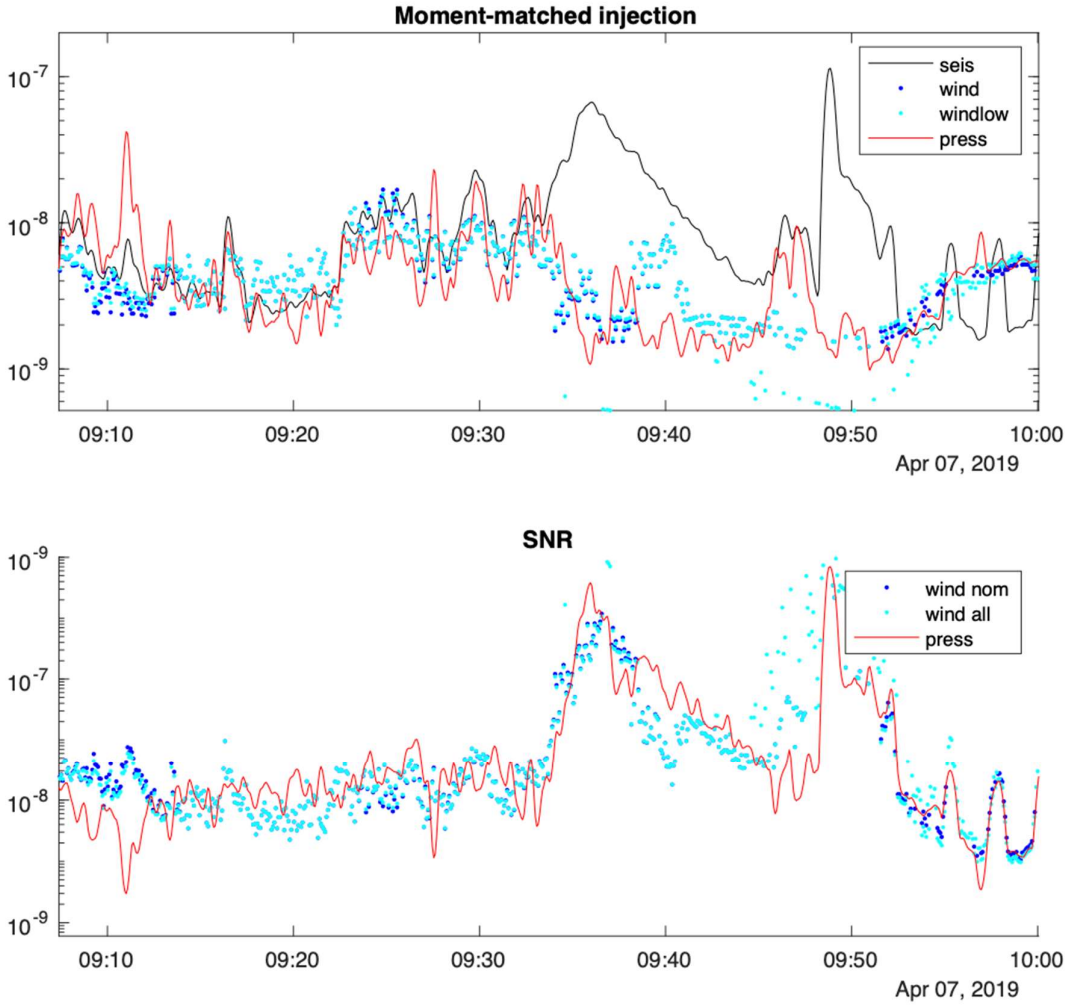

Figure SI1.3: Environmental injection estimation using moment matching of the pressure and seismic signal energies and the wind speed for event S0128a. See text for details.

We match in the log of the signals to de-emphasise the contribution of glitches to the moment calculations and allow for power-law variation. A window length and delay of 1000s are found to produce stable results and corresponds to the typical event length. Figure SI1.3 shows the technique applied to the S0128a event, a large detected during an active period of the sol. The wind speed and pressure energies are reasonably matched to the seismic variation prior to the event, with a divergence apparent as the seismic signal rises above the environmental injection. The signals then converge briefly before a robot arm movement, from 09:48, occurs, demonstrating the ability of the technique to detect non-environmental injection. Two estimates of the wind injection are made, using all the data and masking any measurements below 2.8 m/s. There is generally good agreement between the three estimates though from 09:45 to 09:55 low wind measurements below 2.8 m/s the wind contribution diverges as anomalously low readings cause the contribution to be underestimated.

The lower plot in the figure shows the SNR derived by taking the ratio of the seismic energy to the estimates of the environmental injection. The estimates are similar apart from where low wind readings contribute. An SNR close to unity is seen prior to the event, as the moment matching normalizes the ratio, with a peak value of 1400 for pressure. SNR for all events are given in Table SI1.3.

Comparison of SNR measures

Table SI1.1 shows the SNRZW for all events analyzed in this study and the seismic SNR analysis made with a pre-event time window and the event time window, while Table SI1.2 shows the SNR from spectrogram seismic analysis. Finally, Table SI1.3 contains the SNR derived from environmental co-modulation.

The two poorer SNRWZ events are S0167a and S0189a, but they both have at least the displacement or acceleration SNRWZ larger than 2.25. The 4 best events with a SNRWZ larger than 4 (about 2-sigma away from wind fluctuations) are S0154a, S0133a, S0105a and S0173a. For the 9 events discussed, all SNRZW except S0105a and S0173a are within -50%/+100% of the SNR obtained only from seismic data, made for two different time windows.

Figure SI1.4 shows a comparison of the SNRs from the wind injection from the a priori spectral determinations and the pressure and wind injections for the moment-matching the signals against the seismic estimate. The environmental SNR estimates are expected to be generally similar or lower than the seismic estimates at low SNRs, as environmental injection

is more likely to be a significant part of the signal energy during the event. Higher environmental SNRs are seen for events when environmental injection is generally high but the event was detected during a lull, such as for S0128a, seen in Figure SI1.3. In all cases the environmental estimates reflect the SNR during the event itself, while the seismic estimates necessarily compare the event signal with a nearby quieter period.

For the lower SNR events, when validation is most critical, there is reasonable agreement between all three estimates, with an average ratio of the estimators for all SNRs below 10 being 0.9±0.3.

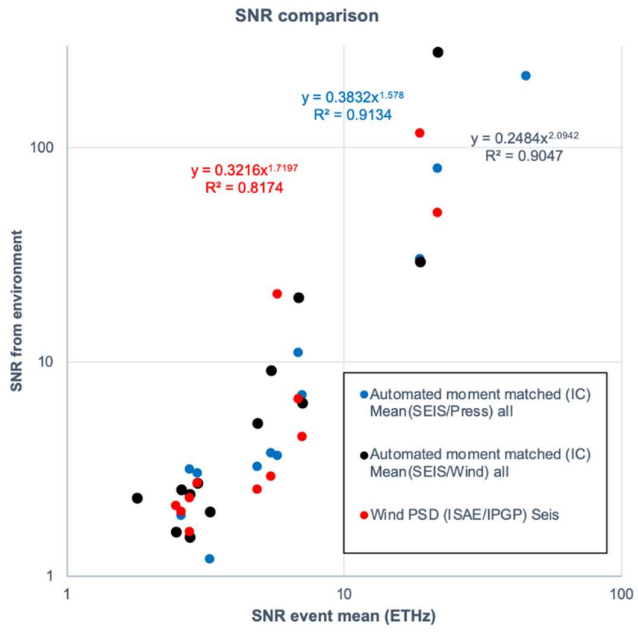

Figure SI1.4: Environmental injection estimations of the event SNR from the wind injection from the a priori spectral determinations and the pressure and wind injections for the moment-matching the signals against the seismic estimates.

SNR application to S0189a event

SNR from wind data: Figure SI1.5 demonstrates the significance of the seismic signal, comparing spectra from the vertical component of the VBB sensor for the event (red) and pre-event background noise (green). Also shown are background spectra for all other times with similar winds (black) and the mean (solid blue) and standard deviation (dashed blue). The event has a clearly anomalously high amplitude peaking far above the 1-sigma level especially for

frequencies above 0.45 Hz, and the background seismic noise is lower than normal. The event has a power signal to noise ratio of 2.5 with respect to these a-priori wind generated noise amplitudes.

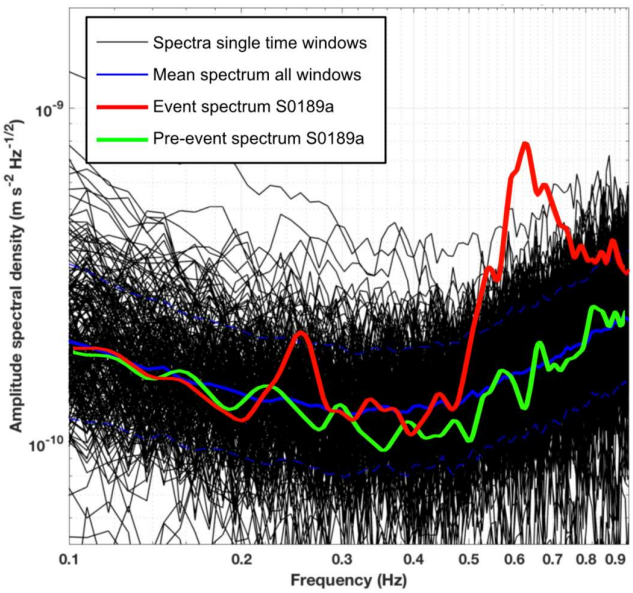

Figure SI1.5 Amplitude spectral density (ASD) of vertical VBB component for the event on Sol 189 (red) compared to ASDs from time windows that have similar wind speed to that recorded during the event (black lines). The blue solid line shows the median ASD of all those time windows. During the event, the squared wind speed was 7(m/s)^2. The green line is the ASD directly before the event, showing that the noise before the event was quite close to the median observed for a squared wind of 6 (m/s)^2. The event red spectrum is far above the 1-sigma fluctuations (dashed blued lines).

SNR from seismic only analysis: this event has signal-to-noise ratios of 10.3, 4.9, 4.3 and 10.3 using peak-to-peak, mean-to-mean, peak P wave and peak S wave amplitudes of spectral envelopes, respectively.

SNR from moment matching of signal energies: Figure SI1.6 compares temporal changes in wind and pressure with the amplitudes of the observed seismic signal. This allows assessment of the contribution from the local environment in the seismic signal during an event and can be quantified by matching the first two moments, mean and variance, of the pressure and seismic energy in the event bandwidth to the wind speed. The matching is done by estimating the

statistical moments over a lagging time window, to avoid matching the statistics during the event. In this analysis, a potential event can be considered of a seismic rather than environmental origin if the seismic signal diverges from the expected match of the two environmental injections. In Figure SI1.6 the seismic energy diverges from the tracked temporal changes in the environmental signals, indicating that the signal source is not due to environmental injection. The seismic energy during the event is significantly above the environmental injection, validating a non-local source for the seismic signal. The wind is shown to vary throughout with a weak periodicity and an aseismic increase in the pressure energy is seen at 05:27 UTC, before the event's arrival. A few locally-generated spikes of energy, or glitches, can also be seen in the seismic signal, dominantly in the East and North components.

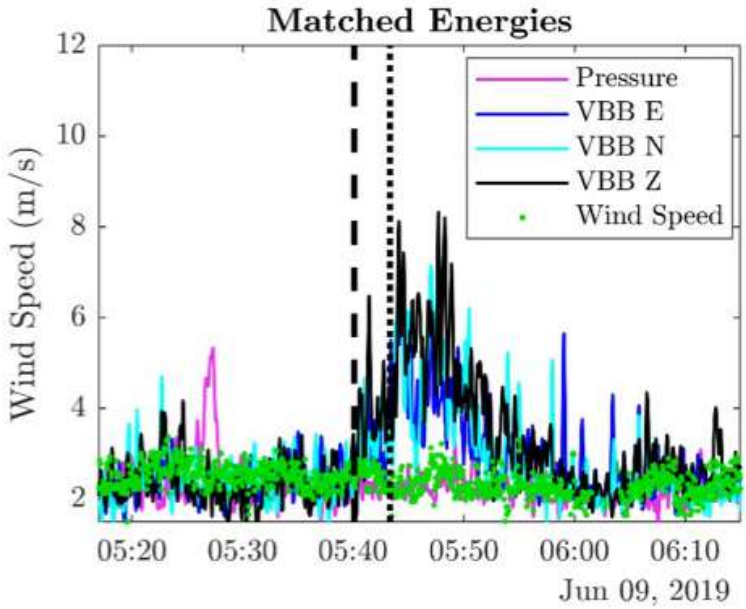

Figure SI1.6 Matched energy summary for the S0189a seismic event. The matched energies for the 3 components of VBB acceleration and pressure are compared to the wind speed. Before and after the event, the VBB acceleration energies in each of the three VBB components follow the same temporal changes in the wind speed, which itself exhibits a weak periodicity in the duration shown. P- and S-wave picks are shown by the vertical black dashed and dotted lines. The seismic event is seen to diverge above the environmental contributions at the time of the P-wave pick.

Table SI1.1: SNR related to wind (SNRZW), as well as mean squared wind, maximum wind in the event window and Seismic SNR for all LF events. SNRZW are either given in displacement or acceleration. All wind squared STD are in the range of 1.3-1.8 $(m/s)^2$, with the exception of S0173 and S0205a for which more stable winds are observed with STD < 0.8 $(m/s)^2$. Values in bold are those above the 2.8 m/s level, for which TWINS has its full resolution. Value in red are those below the 1.8 m/s TWINS resolution threshold. Seismic SNR from acceleration power spectra uses the same frequency range on instrument corrected waveforms.

Event name	**Mean Wind** (m/s)	**Wind std^2** (m/s)^2	**Wind max** (m/s)	**SNRZW** (Displacement)	**SNRZW** (Acceleration)
S0105a (Z)	2,43	1,28	**3,36**	24,4	21,0
S0133a (Z)	2,07	1,8	**3,67**	5,8	8,2
S0154a (Z)	2,53	1,85	**3,8**	3,8	4,4
S0167a (Z)	2,52	1,63	**3,95**	2,5	1,6
S0173a (Z)	**3,47**	0,88	**4.00**	104	116,1
S0183a (Z)	2,19	1,38	**4.38**	2,2	2,3
S0185a (Z)	2,29	1,82	**3.66**	2,7	3,7
S0189a (Z)	2,44	1,55	**3.53**	1,7	2,5
S0205a (Z)	2	0,71	2.11	2,6	2,8
S0226b (Z)	***1,3***	***1,28***	***2.40***	***5***	***4,5***
S0234c (Z)	***1,87***	***0,42***	***2.25***	***1,8***	***2,2***
S0235b (Z)	***0,75***	***0,92***	***2.11***	***78,6***	***148,8***

Table SI1.2: SNR derived from spectral envelopes and acceleration spectra for a selection of HF and LF events. The seismic component used for measuring envelope amplitudes are indicated in parenthesis next to the event names. Signal amplitudes are measured in the envelope time series between signal start and end for the listed frequency range specific to each event, after contamination from glitches are masked. Noise is assumed to be the remaining part of the envelope data.

Event name	SNRs from spectral density envelopes (acceleration)				Signal start (UTC)	Signal end (UTC)	f_{min} (Hz)	f_{max} (Hz)
	Peak signal / peak noise	Mean signal / mean noise	max(P) / peak noise	max(S) / peak noise				
S0105a (Z)	6,8	5,8	4,4	6,8	2019-03-14 20:53:28	2019-03-14 21:28:36	0.31	0.5
S0133a (Z)	11,4	6,9		11,4	2019-04-12 18:04:34	2019-04-12 18:38:48	0.33	0.67
S0154a (Z)	7,9	7,1		7,9	2019-05-04 06:57:28	2019-05-04 07:37:48	0.17	0.67
S0167a (Z)	3,8	2,8		3,8	2019-05-17 16:37:20	2019-05-17 17:13:06	0.18	0.48
S0173a (Z)	94	18,9	35,1	94	2019-05-23 02:12:58	2019-05-23 03:09:54	0.2	0.67
S0183a (Z)	7,5	2,8	7,5	1,9	2019-06-03 02:17:47	2019-06-03 02:48:54	0.33	0.66
S0185a (Z)	14,8	5,5	5,2	14,8	2019-06-05 02:03:25	2019-06-05 02:49:55	0.28	0.83
S0189a (Z)	10,3	4,9	4,3	10,3	2019-06-09 05:30:05	2019-06-09 06:07:57	0.36	0.83
S0205a (Z)	4,5	3	4,5		2019-06-25 16:59:43	2019-06-25 17:26:14	0.29	0.83
S0226b (Z)	5,6	2,6		5,6	2019-07-17 05:33:38	2019-07-17 06:12:49	0.33	0.83
S0234c (Z)	4	2,5	1,6	4	2019-07-25 12:44:18	2019-07-25 13:19:32	0.33	0.83
S0235b (Z)	227,8	21,8	28	227,8	2019-07-26 12:09:16	2019-07-26 13:28:08	0.15	0.91
High frequency events								
S0128a (N)	122,7	45,4		122,7	2019-04-07 09:23:36	2019-04-07 09:55:55	3	7.5
S0218a (N)	9,7	3,3		9,7	2019-07-09 04:53:00	2019-07-09 05:34:45	5	7.5
S0226a (N)	2,3	1,8		2,3	2019-07-17 04:24:18	2019-07-17 04:49:18	3	7.5
S0239a (N)	2,5	2		2,5	2019-07-30 14:16:49	2019-07-30 14:29:52	3	5

Table SI1-3: SNR from moment matching of signal energies.

Event name	Automated moment matched (IC)					
	Peak (SEIS/Press)	Peak(Seis/Wind		Mean(SEIS/Press)	Mean(SEIS/Wind)	
	nominal		all	nominal		all
S0105a (Z)	14	10		3,6	3,3	
S0133a (Z)	**31**	**10**	144	**11**	**7,3**	20
S0154a (Z)	16	9	17	7	8	6,4
S0167a (Z)						
S0173a (Z)	170	160	160	30	29	29
S0183a (Z)	17		*12*	3,1		*2,4*
S0185a (Z)	40		70	3,7	4,6	9
S0189a (Z)	7,4	9,7	13	3,2	4,7	5,1
S0205a (Z)	12		7	3		2,7
S0226b (Z)	3,9		3,9	1,9		2,5
S0234c (Z)	3,1		3,1	1,6		1,6
S0235b (Z)	670		3500	79		280
High frequency events						
S0128a (N)	3400	1400	2,80E+05	214	84	1900
S0218a (N)	2,9	6,5	7,8	1,2	2,1	2
S0226a (N)	4,5		5,3	2,3		2,3

SI2. Interior structure models

The following sections briefly describe how the interior structure models that are used by MQS for locating marsquakes are constructed and how they were used in the location of marsquakes.

The main method for the latter has been described in previous articles (Böse et al., 2016; Khan et al., 2016).

In all, we used 2500 models and to ensure sufficient coverage of the a priori model space, three independent groups from different institutions were solicited for models. Generally, all models were constructed so as to satisfy current observations of mass, moment of inertia, and tidal response. A particular effort was spent on deriving models using different methodologies (thermal history modeling and inversion) and a variety of starting bulk Mars compositions following the approaches detailed in Khan et al. (2018), Rivoldini et al. (2011), Samuel et al. (2019).

Initially, many more models have been considered, but testing showed little difference in resulting marsquake locations, and for the purpose of providing a location in a foreseeable time (on the order of minutes), the initial larger series of models were down-selected to the current set of 2500 models. The current set of models span a relatively large range as shown in Figure SI2.1 and encompasses, among others, all earlier literature models (see eg. Smrekar et al., 2019 for a review) and, consequently, are expected to cover the plausible range of Martian models within which the ``true'' model lies. While this is a reasonable working hypothesis, we nonetheless constantly strive to update and extend the database with models that derive from novel experimental data, methods, and InSight seismic data (Panning et al., 2016). In the following, we briefly describe the main modeling methods and the down-selection procedure and refer the reader for more details to the various studies.

Geodetically-constrained models

The models described in the following are mainly detailed in Rivoldini et al. (2011). The models are spherical, isotropic, non-rotating, and in hydrostatic equilibrium. We assume a convecting and fully liquid iron-sulfur core overlain by a solid silicate mantle and crust. The depth dependent elastic properties of the iron-sulfur alloy in the core are computed following Dumberry & Rivoldini (2015). For the mantle, we consider 5 different compositions (Lodders & Fegley, 1997; Mohapatra & Murty, 2003; Sanloup et al., 1999; Taylor, 2013; Brasser et al., 2018) deduced from the analysis of Martian meteorites. The thermal state of the mantle in our

models is bounded by two end-member ("hottest" and "coldest" profiles) temperature profiles obtained from the thermal evolution study of Plesa et al. (2016). The elastic properties of the mantle are calculated with Perple_X (Connolly, 2009) using the thermodynamic formulation of Stixrude and Lithgow-Bertelloni (2005) and parameters of Stixrude and Lithgow-Bertelloni (2011). For the crust, we use two basaltic chemical compositions (Babeyko & Zharkov, 2000; Khan et al., 2018) either pure or mechanically mixed with a variable amount of periclase. The elastic properties of the basaltic end-members and periclase phase are computed similarly to those of the mantle. To take into account the presence of a low density bed-rock layer and the crustal porosity we amend the computed elastic properties with a pressure dependent function (Khan et al., 2018) that allows for an increase in density from bed-rock at the surface to porosity free material at depth. The closing depth of the porosity and the amount of periclase are chosen such that the average crustal density is in agreement with Wieczorek & Zuber (2004). For the shear attenuation of the silicate shell at 1 s we use PREM (Dziewonski & Anderson, 1981) values at equivalent pressure, i.e., 600 and 140 in the crust and mantle, respectively. Finally, following Rivoldini et al. (2011), the models agree with the observed mass of the planet and to within 3 sigma of the observed moment of inertia value of 0.3638±0.0003 (Konopliv et al., 2016).

Geophysically-constrained models

The models described in the following are obtained from inversion of the most recent set of geophysical data, including mean density (3.9350±0.0012 g/cm^3), mean moment of inertia (0.36379±0.0001), and tidal response (k2=0.169±0.006 and Q=95±10) as described in Khan et al. (2018). Briefly, a set of Martian compositions (Dreibus & Wänke, 1984; Lodders & Fegley, 1997; Sanloup et al., 1999; Taylor, 2013) are explored in the NaO_2-CaO-FeO-MgO-Al_2O_3-SiO_2 model chemical system; a chemical model which accounts for >98% of the mass of the Martian mantle (Dreibus & Wänke, 1984; Bertka and Fei, 1997). Here, Martian mineralogy and physical properties are assumed to be governed by thermodynamic equilibrium and computed for a given model pressure, temperature, and bulk composition along self-consistent adiabats by Gibbs free-energy minimization (Connolly, 2009) using the thermodynamic formulation and parameters of Stixrude & Lithgow-Bertelloni (2005, 2011). The core is assumed to consist of a binary mixture of Fe-S, which is entirely liquid, well-mixed, and convecting. Following the parameterisation of Rivoldini et al. (2011), thermoelastic properties for the core are computed using equations-of-state for liquid iron and liquid iron-sulfur alloys. The crust is likely to be more complex lithologically, not

equilibrated, and is probably porous. The effect of porosity is taken into account by assuming porosity (f) to decrease linearly from <1 at the surface to 0 at the Moho through a decrease in crustal seismic velocity and density by multiplying (1-f) with either seismic property, while crustal composition is fixed to that of Taylor and Maclennan (2009). Shear attenuation and velocity profiles are computed using the laboratory-based grain size- and frequency-dependent viscoelastic model of Jackson & Faul (2010), from which frequency-dependent tidal response functions can be computed. Shear attenuation in the crust and lithosphere is fixed to 600 after PREM (Dziewonski and Anderson, 1981). As for the core, we assume that dissipation only occurs in shear.

Thermal evolution models

The models described in the following are detailed in Samuel et al. (2019). A suite of geodynamically-constrained models was built from running the equivalent of 4.5 Gyr of thermo-chemical evolution of a Mars-like planet. The latter was composed of an adiabatic liquid iron alloy core (with the light element assumed to be sulfur, see Rivoldini et al. (2011), surrounded by a silicate envelope. The silicate envelope consisted of an adiabatic mantle convecting under a stagnant i.e., essentially diffusive) lithospheric lid, the thickness of which including that of a crust enriched in heat-producing elements, evolves with time. The thermo-chemical evolution was computed using a parameterized approach (e.g. Breuer & Spohn, 2006; Hauck & Philipps, 2002) and includes temperature and pressure-dependent mantle viscosity (Samuel et al., 2019; Thiriet et al., 2018) and references therein). By systematically varying six governing parameters within plausible ranges, a collection of thermal profiles was obtained. The parameters are effective activation energy of the mantle, activation volume, reference viscosity, initial mantle temperature under the lithospheric lid, initial core temperature at the core-mantle boundary (CMB), and core radius. The values of all other physical parameters are listed in Samuel et al. (2019) (Table S1.3), with the exception of average mantle and core density, thermal expansion, and specific heat, which were obtained through the successive application of the thermal evolution and the mineral physics model. Cases for which the convective mantle went sub-critical were excluded.

In the crust, body wave velocities and density were assumed to be constant. Crustal density and core sulfur content were varied via bisection to ensure that models satisfy mass and moment of inertia constraints within uncertainties. The uppermost part of the crust consisted of a fixed 2-km-thick bedrock layer with a reduced density and seismic velocities. The geodynamically-computed present-day areotherms were used to determine mantle densities

and seismic velocities with Perple_X (Connolly, 2009) using the thermodynamic formulation of Stixrude & Lithgow-Bertelloni (2005) and parameters of Stixrude & Lithgow-Bertelloni (2011) for the bulk mantle composition of Taylor et al. (2006). Finally, only models with degree-two Love number values (computed following the approach for a linear elastic medium described in Khan et al., 2004) located within the 3-sigma range of the currently observed value 0.169±0.018 (Konopliv et al., 2016), were retained.

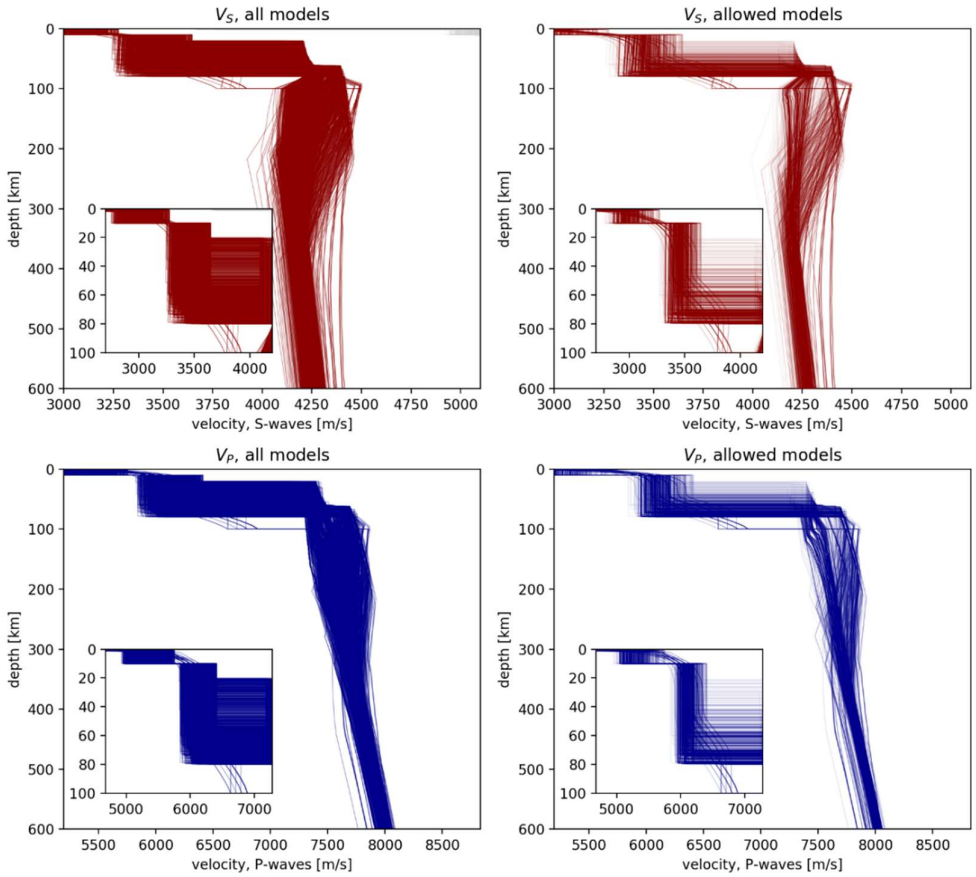

Figure SI2.1: A priori S- and P-wave models used for location of events (left), compared with models compatible with S-P travel time differences of 174±3 s (S0173a) and 157±4 s (S0235b) (right). The extensive S-wave shadow zone in 20-60 degree epicentral distance predicted by many of the a priori models is not compatible with these observations. The allowed models have relatively thick crusts (60-80 km) and a velocity increase or only slight decrease directly below the Moho.

Model down-selection using seismic observations

For locating marsquakes, we perform a grid search over all possible depths, distances, and prior models (Böse et al., 2017; Khan et al., 2016). Measured arrival times relative to an identified P phase are compared to pre-calculated travel times for each combination of depth, distance, and model. Because at most two phases (P and S) corresponding to a single P-S travel time have been identified in the current set of events, interior structure cannot be constrained beyond the prior model range. The events S0235b and S0173a are fortuitous, since they occurred in an epicentral distance range of 26-30 degrees, where many a priori models predict a S-wave shadow zone. The observed P-S arrival time differences of 174±3 seconds (S0173a) and 157±4 seconds (S0235b) therefore allows us to discard 60% of the a priori models (Fig. SI2.1).

SI3. Source characteristics: magnitude and seismic moment, spectral shape

Magnitudes

Magnitude estimates for the 36 low-frequency (LF) and high-frequency (HF) events in the Extended Data Table 1, as well as Table SI3.1 are computed using a modified formulation of that proposed by Böse *et al.* (2018), which calibrated magnitude scales for Mars by simulating the seismic wave propagation through a set of 13 representative 1D Mars models. These scales incorporated pre-mission knowledge on Mars interior structure (Smrekar *et al.*, 2019) and the ambient and instrumental noise that were expected pre-launch (Murdoch *et al.*, 2015a,b; Mimoun *et al.*, 2017). The preliminary seismic data collected by InSight suggest that (1) seismic events on Mars are observable mainly in the frequency band from 2 to 6 s, (2) in some events the arrival of separate energy packets could be interpreted as P- and S-body wave trains, while neither secondary seismic phases nor surface waves could yet be identified, and (3) a class of high-frequency events exists that are mainly visible as an increased excitation of the 2.4 Hz mode. We therefore adapted the Böse *et al.* (2018) method and used 4 different ways of estimating the moment magnitude, depending on event type. All use the epicentral distances, Δ, derived from the travel-time alignment (see main text) for LF events, and derived from Pg-Sg travel time for HF events (with an assumed $v_S = 2$ km/s and $v_P = \sqrt{3}v_S$). The amplitudes were measured depending on the magnitude type:

1. Spectral magnitude $M_{\mathrm{FB}}^{\mathrm{Ma}}$: from spectral amplitude, A_0, which we determined from the plateau of the displacement spectra (Figure 6);
2. Body-wave magnitudes $m_{\mathrm{b}}^{\mathrm{Ma}}$ and $m_{\mathrm{b}S}^{\mathrm{Ma}}$: from the maximum displacement amplitude, A_P or A_S, which we determined in the time window of P- or S-arrivals from the seismograms filtered between 0.2 and 0.5 Hz;
3. 2.4Hz magnitude $M_{2.4\mathrm{Hz}}^{\mathrm{Ma}}$: from the maximum value of the 2.4 Hz amplification peak, which we determined from fitting a Lorenz curve to the displacement spectrum between 2 and 3 Hz.

All magnitudes are calibrated to give a direct estimate of the moment magnitude. For the recalibration of the magnitude scales in Böse *et al.* (2018) we assume a volumetric seismic wave propagation for the LF and a near surface propagation for the HF events. We therefore model the decay of seismic amplitudes for these two groups as 0.9 and 1.1, respectively. These values combine the effects of intrinsic attenuation, geometrical spreading and other propagation effects, and are consistent with the findings in Böse *et al.* (2018). We consider the

spectral magnitude $M_{\mathrm{FB}}^{\mathrm{Ma}}$ to be most reliable and use it as a reference for calibrating the other three scales using events with overlapping amplitude measurements. Details on the procedure and scales will be described in a forthcoming publication. Results for the events described in this paper are shown in Table S5.1.

Spectral estimation

To estimate A_0 for the spectral magnitude and to test whether the events are compatible with tectonic sources, a fit was made using a combination of a Brune source and an attenuation term:

$$A(f) = A_0 A_{\mathrm{src}}(f) A_{\mathrm{att}}(f)$$

The Brune source was estimated (following Brune, 1970) by

$$A_{\mathrm{src}}(f) = \frac{1}{1 + (f/f_c)^2}$$

with the corner frequency f_c

$$f_c = 0.49\beta(\sigma/M_0)^{1/3}$$

estimated from the moment magnitudes in Table S5.1, shear wave velocity β=3 km/s and a stress drop σ=1 MPa. A cursory look at the amplitudes shows that the event's moment magnitudes are below 4, so the expected corner frequency is above 1 Hz for all of the events, and the spectral shape is mainly controlled by attenuation, described by an attenuation term $A_{\mathrm{att}}(f) = \exp(-\pi f\, T/Q_{\mathrm{eff}})$, where T is the estimated travel time of the S-wave and Q_{eff} is an effective quality factor used to explain the spectral shape. The parameters Q_{eff} and A_0 were modified to fit the recorded spectra, while the values for T and M_0 were taken from the aligned distances.

The event spectra are estimated by Welch's method using time windows during the event, compared to noise windows before. The spectra were calculated in Hanning windows of 51.2 seconds length and 50% overlap. Each window was detrended linearly and zero padded by a factor of 4. Spectra were calculated on instrument-corrected and rotated data separately for all components in the ZNE coordinate system. The instrument correction was done to velocity on time windows of two hours to avoid windowing effects in the spectrum estimation. The spectra of the two horizontal channels were averaged. Displacement spectra were calculated by dividing the velocity spectrum by an array containing circular frequencies.

The biggest caveats here are instrument glitches, which are relatively common during the evening period when most events occurred, and create long-period artifacts in the estimated

spectrum. Therefore, for each event, a time window is selected in which no glitches are present with a minimum length of five minutes. Additionally, a noise time window is selected before the event, again avoiding glitches and obvious atmospheric disturbances. For some events, the atmospheric situation before the event was such that no time window could be found. In this case, a time window after the event was selected with a time difference of at least thirty minutes to make sure that only noise was recorded. The exact time windows are shown in Table SI3.1.

The effective quality factor Q_{eff} was estimated manually using the same value for all events in the same distance bin. For the bin around 27° distance, containing the largest events (S0173a, S0235b), Q_{eff} was estimated to be 350 ± 50.

Table SI3.1. Body-wave magnitudes, $m_{\mathrm{b}}^{\mathrm{Ma}}$ and $m_{\mathrm{bS}}^{\mathrm{Ma}}$, 2.4Hz magnitude, $M_{2.4\mathrm{Hz}}^{\mathrm{Ma}}$, and spectral magnitude, $M_{\mathrm{FB}}^{\mathrm{Ma}}$, of all events described in the main text. Preferred magnitude is highlighted in bold. Last four columns show time windows used for spectral computations used to produce Figure 5.

Event name	$m_{\mathrm{b}}^{\mathrm{Ma}}$	$m_{\mathrm{bS}}^{\mathrm{Ma}}$	$M_{2.4\mathrm{Hz}}^{\mathrm{Ma}}$	$M_{\mathrm{FB}}^{\mathrm{Ma}}$	Start signal window (UTC)	End signal window (UTC)	Start noise window (UTC)	End noise window (UTC)
LF events								
S0105a	3.0	3.0	-	**3.2**				
S0133a	3.4	3.1	-	**3.2**				
S0154a	3.6	3.6	-	**3.5**	2019-05-04T07:11:49	2019-05-04T07:14:42	2019-05-04T07:38:19	2019-05-04T07:50:31
S0167a	3.5	3.7	-	**3.8**	2019-05-17T16:52:27	2019-05-17T16:58:05	2019-05-17T16:38:37	2019-05-17T16:46:20
S0173a	3.6	3.5	-	**3.6**	2019-05-23T02:25:51	2019-05-23T02:27:55	2019-05-23T01:54:16	2019-05-23T02:05:17
S0183a	3.3	3.2	-	**3.1**	2019-06-03T02:32:11	2019-06-03T02:34:08	2019-06-03T02:08:07	2019-06-03T02:16:54
S0185a	2.9	3.4	-	**3.1**	2019-06-05T02:20:48	2019-06-05T02:22:45	2019-06-05T03:06:49	2019-06-05T03:17:31
S0189a	2.5	2.7	-	**3.0**				
S0205a	2.8	3.0	-	**3.0**	2019-06-25T17:09:28	2019-06-25T17:10:53	2019-06-25T17:02:47	2019-06-25T17:08:22
S0226b	-	-	-	-	2019-07-17T05:48:44	2019-07-17T05:52:35	2019-07-17T05:21:45	2019-07-17T05:30:04
S0234c	3.2	3.2	-	**2.8**	2019-07-25T12:54:18	2019-07-25T13:09:32	2019-07-25T12:50:00	2019-07-25T12:52:58
S0235b	3.2	3.6	-	**3.6**	2019-07-26T12:21:56	2019-07-26T12:25:51	2019-07-26T12:14:20	2019-07-26T12:18:41
S0325a	3.7	3.7	-	**3.7**	2019-10-26T07:02:57	2019-10-26T07:07:13	2019-10-26T06:55:38	2019-10-26T06:58:39

Table 3.1 cont.

Event name	$m_{\mathrm{b}}^{\mathrm{Ma}}$	$m_{\mathrm{bS}}^{\mathrm{Ma}}$	$M_{2.4\mathrm{Hz}}^{\mathrm{Ma}}$	$M_{\mathrm{FB}}^{\mathrm{Ma}}$	Start signal window (UTC)	End signal window (UTC)	Start noise window (UTC)	End noise window (UTC)
HF events								
S0128a	-	-	1.9	**2.1**	2019-04-07T09:35:05	2019-04-07T09:37:35	2019-04-07T09:10:57	2019-04-07T09:18:33
S0185b	-	-	1.7	**2.0**				
S0202b	-	-	1.5	**1.8**				
S0202c	-	-	1.8	**1.9**				
S0218a	-	-	2.0	**2.3**	2019-07-09T05:08:43	2019-07-09T05:11:51	2019-07-09T04:49:44	2019-07-09T05:00:49
S0222a	-	-	**1.6**	-				
S0226a	-	-	1.2	**1.5**				
S0228c	-	-	1.7	**1.9**				
S0229a	-	-	**1.6**	-				
S0231b	-	-	1.7	**1.9**				
S0234b	-	-	1.3	-				
S0239a	-	-	1.8	**1.9**	2019-07-30T14:22:39	2019-07-30T14:24:19	2019-07-30T14:38:51	2019-07-30T14:50:49
S0246a	-	-	1.7	**1.8**				
S0257a	-	-	**1.8**	-				
S0257b	-	-	**1.7**	-				
S0260a	-	-	2.0	**2.2**	2019-08-21T05:15:52	2019-08-21T05:18:22	2019-08-21T04:48:41	2019-08-21T05:00:05
S0262b	-	-	1.7	**2.2**				
S0263a	-	-	1.4	**1.9**	2019-08-23T11:11:03	2019-08-23T11:12:58	2019-08-23T11:07:27	2019-08-23T11:09:39
S0264e	-	-	2.1	**2.2**	2019-08-25T10:37:52	2019-08-25T10:43:04	2019-08-25T09:56:07	2019-08-25T10:06:54
S0289a	-	-	2.0	**2.3**				
S0290a	-	-	**1.6**	-				
S0291c	-	-	1.7	**2.0**				
S0292a	-	-	1.8	**1.9**				

SI4. Potential volcano-tectonic sources for quakes around InSight

Mars was tectonically active mostly prior 3 Ga (e.g., Golombek and Phillips, 2009), mainly governed by intense volcanic activity associated with extensive surface faulting. While the current tectonic activity on Mars seems negligible, "younger" fault-like structures (initiation age < 2Ma), possibly linked to recent volcanic activities (e.g. Neukum et al., 2004; Vaucher et al., 2009) represent potential sources of marsquakes.

Major geological features are well observed at the surface of Mars from orbital data (MRO, MeX, MGS, Odyssey). We show on Figure SI6.1 the main tectonic/volcanic structures in an area covering up to 70° epicentral distance from the InSight lander, where most of the quakes are located (see main text and Supplement S1). Note that we focus mainly on major extensive structures that correspond to large crustal features mostly associated with deeper processes. We thus do not describe small and surficial reverse faulting scattered over the globe (black lines on Figure SI6.1).

The closest (10° to 40° distance) and largest structure near InSight is Elysium Mons (see Figure SI4.1), a volcanic bulge associated with large dike-induced grabens situated near its apex (see Figure SI4.1) and on its southeastern flank (Cerberus Fossae and Grjótá Valles). Based on boulders and landslide distributions along the fossae, Roberts et al. (2012) and Brown & Roberts (2019) have shown that those large structures might have experienced several marsquakes in the past. Assuming that the Cerberus Fossae system is currently active (Taylor et al., 2013) and that its direction of long-term propagation is toward the East, the source of quakes would preferably be located on the eastern part of the system, where fossae are supposedly younger (i.e. propagating fault/dike tip), and thus hosting higher stress concentrations (see Green et al., 2015; Rubin & Gillard, 1998; Sigmundsson et al., 2015 for terrestrial examples).

Provided that these dike systems are active and genetically linked to Elysium Mons, quakes and tremors may be triggered by volcanic activity, which is supported by crater counting and relative stratigraphy with recent possible activity as recent as 2.5-3 Myr (Vaucher et al., 2009). A secondary vent is also observed in the North (Hecates Tholus) with normal faults and grabens (Galaxias Fossae).

At greater distance (> 40°), we identify several other structures that might be responsible for quakes (Figure SI4.1): i) the large Nili Fossae in the West, at the edge of the Isidis basin formed by impact more than 3 Ga ago (Greeley and Guest, 1987), which could still present surface

instabilities leading to landslides or rockfalls; ii) in the East, the Tharsis Bulge is associated to far-field faults and overflow systems of Sirenum, Memnonia or Mangala Fossae, where late geological activity can be expected (Anderson et al., 2019); iii) the Hellas Basin region in the Southwest, where possible slope destabilizations of the basin rims might occur. Furthermore, the large regional gravity anomaly in the vicinity of Hellas could possibly be responsible for quakes, as relaxation of ancient stress field might occur due to a significant change in the crustal thickness (from 60 km in Noachis Terra to 10-15 km in Hellas Planitia; Genova et al., 2016), associated with crustal lateral heterogeneities.

Finally, the Martian crustal dichotomy could be at the origin of local landslides and slope destabilizations (e.g., Lefort et al., 2015), with the Southern highland terrains situated 1-3km higher in elevation than the Northern lowlands, and with possibly large crustal thickness variations from 55±20 km in the South to 32 km in the North (according to Zuber et al., 2000).

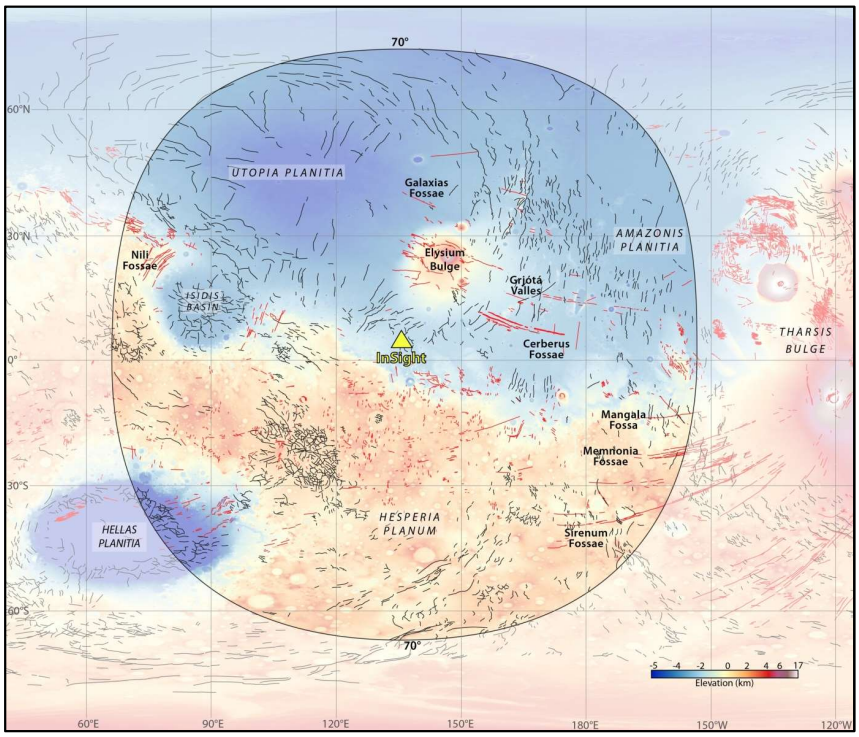

Figure SI4.1: Regional fault map of Mars and main potential sources of quakes in a 70° epicentral distance range from the InSight lander (yellow triangle). The global fault map is modified from the compilation of Knapmeyer et al., 2006. Black lines represent reverse/strike slip faults and red lines are normal faults.

References

Anderson, R. C., Dohm, J. M., Williams, J. P., Robbins, S. J., Siwabessy, A., Golombek, M. P., & Schroeder, J. F. (2019). Unraveling the geologic and tectonic history of the Memnonia-Sirenum region of Mars: Implications on the early formation of the Tharsis rise. *Icarus*. https://doi.org/10.1016/j.icarus.2019.06.010

Babeyko, A. Y., & Zharkov, V. N. (2000). Martian crust: a modeling approach. *Physics of the Earth and Planetary Interiors*, *117*(1–4), 421–435. https://doi.org/10.1016/S0031-9201(99)00111-9

Banfield, D., Rodriguez-Manfredi, J.A., Russell, C.T., K. M. Rowe, D. Leneman, H. R. Lai, et al. (2019). InSight Auxiliary Payload Sensor Suite (APSS), *Space Sci Rev*., 215: 4. https://doi.org/10.1007/s11214-018-0570-x

Banfield, D., A. Spiga et al. (2019)The atmosphere of Mars, as seen by InSight. *Nature Geoscience*, this issue.

Böse, M., Clinton, J. F., Ceylan, S., Euchner, F., van Driel, M., Khan, A., et al. (2017). A Probabilistic Framework for Single-Station Location of Seismicity on Earth and Mars. *Physics of the Earth and Planetary Interiors*, *262*, 48–65. https://doi.org/10.1016/j.pepi.2016.11.003

Böse, M., Giardini, D., Stähler, S., Ceylan, S., Clinton, J., van Driel, M., et al. (2018). Magnitude scales for Marsquakes, Bull. Seis. Soc. Am. 108(5A), 2764-2777, doi:10.1785/01201180037.

Breuer, D., & Spohn, T. (2006). Viscosity of the Martian mantle and its initial temperature: Constraints from crust formation history and the evolution of the magnetic field. *Planetary and Space Science*, *54*(2), 153–169. https://doi.org/10.1016/J.PSS.2005.08.008

Brown, J. R., & Roberts, G. P. (2019). Possible evidence for variation in magnitude for marsquakes from fallen boulder populations, Grjota Valles, Mars. *Journal of Geophysical Research: Planets*, 124, 801– 822. https://doi.org/10.1029/2018JE005622.

Brune, J. N. (1970). Tectonic stress and the spectra of seismic shear waves from earthquakes, J. Geophys. Res., 75(26), 4997–5009, doi:10.1029/JB075i026p04997.

Clinton, J., Giardini, D., Böse, M., Ceylan, S., van Driel, M., Euchner, F. et al. (2018). The Marsquake Service: Securing Daily Analysis of SEISData and Building the Martian Seismicity Catalogue for InSight. *Space Science Review,* https://doi.org/10.1007/s11214-

018-0567-5.

Connolly, J. A. D. (2009). The geodynamic equation of state: What and how. *Geochemistry, Geophysics, Geosystems*, *10*(10), Q10014. https://doi.org/10.1029/2009GC002540

Dreibus, G., & Wänke, H. (1984). Accretion of the Earth and the inner planets. In *Proceedings of the 27th International Geological Congress* (Vol. 11, pp. 1–20).

Dumberry, M., & Rivoldini, A. (2015). Mercury's inner core size and core-crystallization regime. *Icarus*, *248*, 254–268. https://doi.org/10.1016/j.icarus.2014.10.038

Dziewonski, A. M., & Anderson, D. L. (1981). Preliminary reference Earth model. *Physics of the Earth and Planetary Interiors*, *25*(4), 297–356. https://doi.org/10.1016/0031-9201(81)90046-7

Genova, A., Goossens, S., Lemoine, F., Mazarico, E., Neumann, G., Smith, D. & Zuber, M. (2016). Seasonal and static gravity field of Mars from MGS, Mars Odyssey and MRO radio science, *Icarus*, Volume 272. doi: 10.1016/j.icarus.2016.02.050

Golombek, M., & Phillips, R. (2009). Mars tectonics. In T. Watters & R. Schultz (Eds.), Planetary Tectonics (Cambridge Planetary Science, pp. 183-232). Cambridge: Cambridge University Press. doi:10.1017/CBO9780511691645.006

Greeley, R. & Guest, J.E. (1987). Geologic map of the eastern equatorial region of Mars: U.S. Geological Survey Miscellaneous Investigations Series Map I-1802-B, scale 1:15,000,000.

Green, R. G., Greenfield, T., White, R. S. (2015). Triggered earthquakes suppressed by an evolving stress shadow from a propagating dike. *Nature Geoscience*, *8*(8), 629–632. https://doi.org/10.1038/ngeo2491

Hauck, S. A., & Philipps, R. (2002). Thermal and crustal evolution of Mars. *Journal of Geophysical Research*, *107*(E7), 5052. https://doi.org/10.1029/2001JE001801

Jackson, I., & Faul, U. H. (2010). Grainsize-sensitive viscoelastic relaxation in olivine: Towards a robust laboratory-based model for seismological application. *Physics of the Earth and Planetary Interiors*, *183*(1), 151–163, https://doi.org/https://doi.org/10.1016/j.pepi.2010.09.005

Khan, A., Mosegaard, K., Williams, J. G., & Lognonné, P. (2004). Does the Moon possess a molten core? Probing the deep lunar interior using results from LLR and Lunar Prospector. *Journal of Geophysical Research (Planets)*, *109*, 9007.

https://doi.org/10.1029/2004JE002294

Khan, A., van Driel, M., Böse, M., Giardini, D., Ceylan, S., Yan, J., et al. (2016). Single-station and single-event marsquake location and inversion for structure using synthetic Martian waveforms. *Physics of the Earth and Planetary Interiors*, *258*, 28–42. https://doi.org/10.1016/j.pepi.2016.05.017

Khan, A., Liebske, C., Rozel, A., Rivoldini, A., Nimmo, F., Connolly, J. A. D., et al. (2018). A Geophysical Perspective on the Bulk Composition of Mars. *Journal of Geophysical Research: Planets*, 1–37. https://doi.org/10.1002/2017JE005371

Knapmeyer, M., Oberst, J., Hauber, E., Wählisch, M., Deuchler, C. & Wagner, R. (2006). Working models for spatial distribution and level of Mars' seismicity. . *Journal of Geophysical Research: Planets* 111, 1–23. doi:10.1029/2006JE002708.

Konopliv, A. S., Park, R. S., & Folkner, W. M. (2016). An improved JPL Mars gravity field and orientation from Mars orbiter and lander tracking data. *Icarus*, *274*, 253–260.

Lefort, A., Burr, D. M., Nimmo, F. & Jacobsen, R. E. (2015). Channel slope reversal near the Martian dichotomy boundary: Testing tectonic hypotheses. *Geomorphology*, 240, 121-136. https://doi.org/10.1016/j.geomorph.2014.09.028

Lodders, K., & Fegley, B. (1997). An Oxygen Isotope Model for the Composition of Mars. *Icarus*, *126*(2), 373–394. https://doi.org/10.1006/ICAR.1996.5653

Lognonné et al. (2020). First constraints on the shallow elastic and anelastic structure of Mars from InSight data. *Nature Geoscience*, this issue.

Mimoun, D., Murdoch, N., Lognonné, P., Hurst, K., Pike, W.T., Hurley, J., Nebut, T. & Banerdt, W.B. (2017). The Noise Model of the SEIS Seismometer of the InSight Mission to Mars, *Space Science Review*, doi: 10.1007/s11214-017-0409-x.

Mohapatra, R. K., & Murty, S. V. (2003). Precursors of Mars: Constraints from nitrogen and oxygen isotopic compositions of martian meteorites. *Meteoritics & Planetary Science*, *38*, 225–241. doi;10.1111/j.1945-5100.2003.tb00261.x

Murdoch, M., Mimoun, D., Lognonné, P.H., and SEIS science team (2015a). SEIS performance model environment document, Tech. rep., ISGH-SEIS-JF-ISAE-030.

Murdoch, M., Mimoun, D., Lognonné, P.H., and SEIS science team (2015b). SEIS performance budgets, Tech. rep., ISGH-SEIS-JF- ISAE-0010.

Murdoch, N., Mimoun, D., Garcia, R.F., Rapin, W., Kawamura, T., Lognonné, P., Banfield, D. & Banerdt, W.B. (2017). Evaluating the Wind-Induced Mechanical Noise on the InSight Seismometers, *Space Science Review*, 211, 429-455, doi:10.1007/s11214-016-0311-y.

Neukum, G., Jaumann, R., Hoffmann, H., Hauber, E., Head, J.W., Basilevsky, et al. (2004). Recent and episodic volcanic and glacial activity on Mars revealed by the High Resolution Stereo Camera. *Nature* 432, 971–979. doi:10.1038/nature03231

Panning, M. P. et al. (2017), Planned Products of the Mars Structure Service for the InSight Mission to Mars, *Space Sci. Rev.*, *211*(1), 611–650, doi:10.1007/s11214-016-0317-5.

Plesa, A.-C., Grott, M., Tosi, N., Breuer, D., Spohn, T., & Wieczorek, M. A. (2016). How large are present-day heat flux variations across the surface of Mars? *Journal of Geophysical Research: Planets*, *121*(12), 2386–2403. https://doi.org/10.1002/2016JE005126

Rivoldini, A., Van Hoolst, T., Verhoeven, O., Mocquet, A., & Dehant, V. (2011). Geodesy constraints on the interior structure and composition of Mars. *Icarus*, *213*(2), 451–472. https://doi.org/10.1016/j.icarus.2011.03.024

Rubin, A. M., & Gillard, D. (1998). Dike-induced earthquakes: Theoretical considerations. *Journal of Geophysical Research*, 103(1), 17–30.

Samuel, H., Lognonné, P., Panning, M. P., & Lainey, V. (2019). The rheology and thermal history of Mars revealed by the orbital evolution of Phobos. *Nature*, *569*(7757), 523–527. https://doi.org/10.1038/s41586-019-1202-7

Sanloup, C., Jambon, A., & Gillet, P. (1999). A simple chondritic model of Mars. *Physics of the Earth and Planetary Interiors*, *112*(1–2), 43–54. https://doi.org/10.1016/S0031-9201(98)00175-7

Sigmundsson, F., Hooper, A., Hreinsdóttir, S., Vogfjörd, K. S., Ófeigsson, B. G., Heimisson, E. R., et al. (2015). Segmented lateral dike growth in a rifting event at Bárðarbunga volcanic system, Iceland. *Nature*, 517(7533), 191–195. https://doi.org/10.1038/nature14111

Smrekar, S. E., Lognonné, P., Spohn, T., Banerdt, W. B., Breuer, D., Christensen, U., et al. (2019). Pre-mission InSights on the Interior of Mars. *Space Science Reviews*, *215*(1), 3. https://doi.org/10.1007/s11214-018-0563-9

Stixrude, L., & Lithgow-Bertelloni, C. (2005). Thermodynamics of mantle minerals - I.

Physical properties. *Geophysical Journal International*. https://doi.org/10.1111/j.1365-246X.2005.02642.x

Stixrude, L., & Lithgow-Bertelloni, C. (2011). Thermodynamics of mantle minerals - II. Phase equilibria. *Geophysical Journal International*, *184*, 1180–1213. https://doi.org/10.1111/j.1365-246X.2010.04890.x

Taylor, G. J. (2013). The bulk composition of Mars. *Chemie der Erde - Geochemistry*, *73*(4), 401–420. https://doi.org/10.1016/J.CHEMER.2013.09.006

Taylor, G. J., Stopar, J. D., Boynton, W. V, Karunatillake, S., Keller, J. M., Brückner, J., et al. (2006). Variations in K/Th on Mars. *Journal of Geophysical Research*, *112*(E3), E03S06. https://doi.org/10.1029/2006JE002676

Taylor, J., Teanby, N. A., & Wookey, J. (2013). Estimates of seismic activity in the Cerberus Fossae region of Mars. *Journal of Geophysical Research: Planets*, 118(12), 2570-2581.

Taylor, S. R. (1980). Refractory and moderately volatile element abundances in the earth, moon and meteorites. In S. A. Bedini (Ed.), *Lunar and Planetary Science Conference Proceedings* (Vol. 11, pp. 333–348).

Thiriet, M., Michaut, C., Breuer, D., & Plesa, A.-C. (2018). Hemispheric Dichotomy in Lithosphere Thickness on Mars Caused by Differences in Crustal Structure and Composition. *Journal of Geophysical Research: Planets*. https://doi.org/10.1002/2017JE005431

Vaucher, J., Baratoux, D., Mangold, N., Pinet, P., Kurita, K., & Grégoire, M. (2009). The volcanic history of central Elysium Planitia: Implications for martian magmatism. *Icarus*, Volume 204. doi: 10.1016/j.icarus.2009.06.032.

Wieczorek, M. A., & Zuber, M. T. (2004). Thickness of the Martian crust: Improved constraints from geoid-to-topography ratios. *Journal of Geophysical Research*, *109*(E1), E01009. https://doi.org/10.1029/2003JE002153

Zuber, M., Solomon, S., Phillips, R., Smith, D., Tyler, L., Aharonson, O., et al. (2000). Internal Structure and Early Thermal Evolution of Mars from Mars Global Surveyor Topography and Gravity, *Science*, Volume 287. doi: 10.1126/science.287.5459.1788.